

Heavy Higgs Boson Production in Association with Three Jets at Hadron Supercolliders

Adam Duff and Dieter Zeppenfeld

Department of Physics, University of Wisconsin, Madison, WI 53706

Abstract

We consider the real emission QCD correction to heavy Higgs boson production via weak boson fusion in high energy pp collisions. The $\mathcal{O}(\alpha_s)$ corrections are determined for the complete electroweak $qq \rightarrow qqW^+W^-$ process. The presence of a third parton in the final state affects the formation of rapidity gaps only slightly. In particular, soft emission into the gap region is severely suppressed. Also, we investigate how the additional hard emission affects forward-jet-tagging and central-jet-vetoing efficiencies in the search for $H \rightarrow W^+W^- \rightarrow \ell^+\nu\ell^-\bar{\nu}$ decays.

I. INTRODUCTION

One of the prime objectives of experiments at hadron supercolliders is the discovery of the Higgs boson and the subsequent investigation of its properties. If the Higgs boson is relatively heavy or if electroweak symmetry breaking is driven by some new strong interactions, then the study of Higgs boson production in the weak boson fusion process or of longitudinal weak boson scattering becomes particularly important.

The study of the “gold-plated” $ZZ \rightarrow \ell^+\ell^-\ell^+\ell^-$ Higgs boson decay mode alone will clearly not suffice to completely understand the nature of electroweak symmetry breaking or may not yield a significant signal [1]. Because of severe background problems one needs to utilize as much information as possible about the full structure of the underlying $qq \rightarrow qqVV$ process when trying to utilize other channels like $W^+W^- \rightarrow \ell^+\nu\ell^-\bar{\nu}$ or hadronic decays of the produced weak bosons. This includes forward-jet-tagging [2–4] to suppress processes like $q\bar{q} \rightarrow VV$, central-jet-vetoing for the reduction of top-quark backgrounds [4], looking for relatively low overall hadronic multiplicities [5] or searching for rapidity gap signatures [6,7] to exploit the color singlet exchange between the two initial state quarks as a distinguishing feature of the signal. In all these cases the knowledge of QCD emission corrections is important or even crucial to assess the acceptance of the various procedures for signal events.

In this paper we present first results of the calculation of all $\mathcal{O}(\alpha_s)$ real emission corrections to the full electroweak process $qq \rightarrow qqWW$ (and crossing related ones) with subsequent leptonic W decays. Results are obtained by the numerical evaluation of polarization amplitudes [8,9] and were implemented for pp and $p\bar{p}$ collisions. An outline of the calculation is given in Section II, details are relegated to an Appendix.

In two subsequent Sections we apply this calculation to two of the issues mentioned above. The suppression of QCD radiation into the central rapidity region is investigated in Section III. Color coherence between initial and final state radiation off each of the incoming quarks and the absence of color transfer between the two quark lines in the $qq \rightarrow qqWW$ process leads to strongly suppressed radiation into the rapidity range between the two final

state quarks. This confirms the expectation that rapidity gaps, *i.e.* regions of very low hadronic activity, may form between the two quark jets. The influence of processes with gluons in the initial state (*e.g.* $gq \rightarrow q\bar{q}qWW$) on the radiation pattern and the effect of radiation on the average gap width are analyzed here.

In Section IV we then investigate the effects of QCD radiation on forward-jet-tagging and central-jet-vetoing as discussed in Ref. [4]. Because of the additional jet activity the efficiency of a central-jet-veto might be severely affected by higher order QCD corrections. We show that this is indeed the case for the electroweak background of transverse W production, but not for the heavy Higgs signal itself. We calculate the signal acceptance of the tagging and vetoing techniques and find, typically, a 15% reduction of signal rates compared to the lowest order results.

II. CALCULATIONAL METHODS

The processes which need to be considered are the QCD real emission corrections to weak boson scattering. In the on-shell approximation for the produced W 's this corresponds to the cross section evaluation at order $\mathcal{O}(\alpha_s\alpha_{QED}^4)$, *i.e.* at tree level, of the complete process

$$q_1q_2 \rightarrow q_3q_4 W^+W^- g \quad (1)$$

and all crossing related processes, like, *e.g.*,

$$gq_1 \rightarrow q_3\bar{q}_2q_4 W^+W^- . \quad (2)$$

Some representative Feynman graphs are shown in Fig. 1 and the full set of contributing graphs is outlined in the Appendix. We are primarily interested in the weak boson scattering process as depicted in Figs. 1a and b. However, when trying to calculate the distributions of the final state quarks we need to treat the incoming weak bosons as off-shell particles. Electromagnetic gauge invariance then requires to consider the t -channel photon exchange of Fig. 1b together with W bremsstrahlung off the two quark lines. We are thus lead to consider

the full $\mathcal{O}(\alpha_s \alpha_{QED}^4)$ process, including all W bremsstrahlung processes off the external quark lines, as shown, for example, in Fig. 1c.

Questions of electromagnetic gauge invariance do not arise when considering the s -channel Higgs resonance only, as depicted in Fig. 1a. For a simplified definition of the Higgs boson signal we shall also consider these “ s -channel resonance” contributions in isolation. It is well known, however, that for a large Higgs boson width, *i.e.* in the case of a heavy Higgs boson, the resonance contribution overestimates the production cross section of longitudinal W 's at large values of the W pair invariant mass [10]. The “ s -channel resonance” contributions should therefore only be taken as a qualitative estimate of the Higgs boson signal. As an alternative means of isolating the effects of a heavy Higgs boson or of the scattering of longitudinal weak bosons we shall also consider the cross section difference $\sigma(m_H) - \sigma(m_H = 100 \text{ GeV})$, *i.e.* the excess events over a light Higgs boson scenario.

The lowest order process, without the gluon emission considered here, has been calculated by several groups [10,4]. We obtain the real emission QCD corrections by numerically evaluating the amplitudes, using the helicity amplitude calculus of Ref. [9] as implemented in the HELAS package [8]. Fermion masses are neglected everywhere. When considering leptonic W -decays the W propagator factors are taken in the narrow width approximation in order to eliminate additional Feynman graphs which are required by gauge invariance for off-shell W 's. Details are given in the Appendix.

A simple Breit-Wigner resonance form with a constant width in the timelike region is used for the Higgs boson propagator. Refinements can be made [11], but they are not relevant in the following since we are primarily interested here in the QCD structure of weak boson fusion processes and do not aim at a precise modeling of the SM prediction for $W^+W^- + 3$ jet production. Finally, the phase space integrals over the squared amplitudes are performed with the VEGAS integration package [12]. For the parton densities inside the proton we use set D'_- of Ref. [13] and we choose the geometric mean of the final state parton transverse momenta as the scale of the structure functions and of the strong coupling constant $\alpha_s(Q^2)$.

Because we are working in the Born approximation and since we are using massless quarks throughout, the total cross section for $pp \rightarrow W^+W^-X$ comes out to be divergent and we need to impose acceptance cuts to obtain finite results.

t -channel photon exchange as shown in Fig. 1c is singular at low Q^2 and in addition the parton model no longer provides an adequate description in this phase space region. Rather, one should use measured electromagnetic form factors of the proton. While a proper treatment of low Q^2 photon exchange is possible [14] one finds that this region can safely be neglected when considering signatures for weak boson scattering [3]. Hence, we only consider the deep inelastic scattering region in the following by imposing the cut $|Q^2| > 4 \text{ GeV}^2$.

Annihilation diagrams contribute in processes with identical flavors on the two quark lines. An example is shown in Fig. 1d. Here the splitting of the s -channel photon into a $q\bar{q}$ pair diverges at small dijet invariant masses. Again this process is unimportant for the weak boson scattering regime in which we are interested. We eliminate the singularity by requiring $m_{jj} > 10 \text{ GeV}$ for all pairs of final state partons. Finally, collinear singularities, which arise from initial state gluon radiation, are avoided by considering partons of finite transverse momentum only.

These cuts eliminate all numerical divergencies. They are largely superseded by the acceptance cuts which will be made in actual experiments. Throughout the following we require that all pairs of partons which satisfy the jet-identification requirements (typically $p_T > 40 \text{ GeV}$ and a limited range in pseudorapidity) are well separated in the pseudorapidity–azimuthal angle plane,

$$R_{jj} = (\Delta\eta_{jj}^2 + \Delta\phi_{jj}^2)^{\frac{1}{2}} > 0.7, \quad (3)$$

and similarly that all decay leptons are isolated,

$$R_{\ell j} = (\Delta\eta_{\ell j}^2 + \Delta\phi_{\ell j}^2)^{\frac{1}{2}} > 0.7. \quad (4)$$

Additional requirements on jet and lepton transverse momenta and on the angular acceptance will be listed separately in the following sections.

We will want to study the effects of the $\mathcal{O}(\alpha_s)$ QCD corrections on one and two jet inclusive distributions and we would like to use the code to assess the probability of soft radiation into the rapidity interval defined by two tagging jets. A complete calculation of such observables would require the determination of virtual effects and the resummation of soft gluon emission, tasks which are clearly beyond the scope of the present paper. Instead we use the “truncated shower approximation” (TSA) to obtain estimates of these observables [15].

In the TSA we replace the tree level differential cross section for three parton final states, $d\sigma(WWjjj)_{\text{TL}}$, by

$$d\sigma(WWjjj)_{\text{TSA}} = d\sigma(WWjjj)_{\text{TL}} \left(1 - e^{-p_{Tj,\text{min}}^2/p_{t\text{sa}}^2}\right), \quad (5)$$

Here $p_{Tj,\text{min}}$ is the smallest transverse momentum of the three final state partons. As $p_{Tj} \rightarrow 0$ the final factor in Eq. (5) acts as a regulator of the small p_T singularity. The TSA parameter $p_{t\text{sa}}$ is chosen to reproduce the lowest order cross section within a given set of acceptance cuts. For the full electroweak process the singularities associated with low Q^2 photon exchange would introduce a very strong dependence of $p_{t\text{sa}}$ on the phase space region which is considered. This is not the case, however, for the Higgs boson signal as defined by the “ s -channel resonance” contribution. It is well known that the K -factor for the $qq \rightarrow qqH$ process is close to unity [16] and this process has a finite total cross section at tree level. By choosing $p_{t\text{sa}}$ such that the “ s -channel resonance” contribution to $\sigma(WWjjj)_{\text{TSA}}$ reproduces the corresponding lowest order cross section, we obtain an algorithm which agrees with the full $\mathcal{O}(\alpha_s\alpha_{QED}^4)$ calculation in the 3 jet phase space region, which allows to study 1-jet and 2-jet inclusive distributions to the same order, and which provides an excellent approximation to these distributions and to the overall normalization at full $\mathcal{O}(\alpha_s\alpha_{QED}^4)$ in the phase space region where the Higgs resonance dominates.

Anticipating the acceptance cuts to be used below, we have determined the TSA parameter by matching the total Higgs production cross sections in pp scattering at $\sqrt{s} = 40$ TeV with one or two visible jets exceeding a minimal transverse momentum. Results are given in Table I. One finds that $p_{t\text{sa}}$ is quite insensitive to the value of the Higgs boson mass and also

varies very little with the $p_{Tj,min}$ cut imposed in the 1-jet inclusive case. When requiring the presence of two partons of $p_T > 20, 40, \text{ or } 60$ GeV this variation is somewhat stronger, but even here the variation in $p_{t_{sa}}$ of $\approx \pm 1$ GeV corresponds to normalization changes of the cross section by up to 30% only, which is within the uncertainty range of our tree level calculation.

III. COLOR STRUCTURE AND RAPIDITY GAPS

The characteristic features of the $\mathcal{O}(\alpha_s)$ emission corrections to weak boson scattering can be understood in terms of the color structure of the lowest order process. In the dominant t -channel contributions (see Figs. 1a–c) no color is exchanged between the two incoming quarks (or anti-quarks). For small scattering angles of these incoming fermions the color charges are accelerated rather little and the resulting “synchrotron radiation” of gluons occurs predominantly into the forward direction, between the beam axis and the direction of the scattered (anti)quark. One thus expects very little hadronic activity to arise from bremsstrahlung off the hard process in the central region, between the two scattered quarks. Since the energy carried by the quarks is typically much larger than the virtuality of the emitted weak bosons (of $\mathcal{O}(m_W)$) these quarks are produced at rather large pseudorapidities, leaving a wide rapidity region with suppressed radiation [6]. This pattern is fundamentally different from the one expected for typical background processes (like *e.g.* $gg \rightarrow t\bar{t} \rightarrow b\bar{b}W^+W^-$) where color exchange between the two incoming partons leads to strong gluon radiation into all regions of the legoplot.

The suppressed radiation into the central region may then lead to the formation of rapidity gaps, pseudorapidity regions of very low or no hadronic activity except for the Higgs decay products [6,7]. This rapidity gap may be filled, however, by hadrons from the underlying event [17] and the full formation of the gap is expected to be observable only in a small fraction of all signal events where fluctuations or the absence of multiple parton interactions make the radiation pattern of the hard scattering process visible [7,18,19].

Here we do not discuss this last question of the gap survival probability any further, rather we investigate whether the higher order QCD corrections indeed do lead to the radiation patterns suggested by the color flow arguments. Processes with three quarks in the final state (like *.e.g* $gq \rightarrow q\bar{q}qH$) might substantially alter the expected pattern. In addition, a precise knowledge of the radiation in signal vs. background events may help to distinguish the two even in the presence of an underlying event [5].

The features of the heavy Higgs boson signal discussed above suggest a search following the strategy developed for rapidity gap events in Ref. [20]. We study 2 jet inclusive WW events where both W 's decay leptonically and where the two charged decay leptons fall into the central rapidity region between the two tagging jets. More precisely we start with events containing two charged leptons of high transverse momentum in the central region,

$$p_{T\ell} > 100 \text{ GeV}, \quad |\eta_{\ell}| < 2. \quad (6)$$

No hadronic jet with transverse momentum

$$p_{Tj} > 40 \text{ GeV} \quad (7)$$

is allowed in the pseudorapidity interval between the two leptons. On either side of the lepton pair we search for the first jet of $p_{Tj} > 40 \text{ GeV}$, *i.e.* we require the presence of two tagging jets. The pseudorapidity range between the tangents to the jet definition cones (of radius $R = 0.7$) is called the “gap region” and the two charged leptons are required to fall into this gap region. Denoting by $\eta_{j_1} < \eta_{j_2}$ the pseudorapidities of the two tagging jets we thus require

$$\eta_{j_1} + 0.7 < \eta_{\ell^+}, \eta_{\ell^-} < \eta_{j_2} - 0.7. \quad (8)$$

The width of the gap region is denoted by

$$y_{gap} = |\eta_{j_1} - \eta_{j_2}| - 2 \cdot 0.7. \quad (9)$$

The average gap width is expected to be large for weak boson scattering events but not necessarily in the phase space region where W bremsstrahlung dominates. This is confirmed

in Fig. 2 where $d\sigma/dy_{gap}$, within the acceptance requirements of Eqs. (6)–(8), is shown for the production of a $m_H = 800$ GeV Higgs boson in pp collisions at $\sqrt{s} = 40$ TeV. The Higgs boson and longitudinal weak boson scattering contributions can be isolated by comparing with the case of a very light Higgs boson, taken here as $m_H = 100$ GeV. For the lepton acceptance requirements of Eq. (6) the resonance contribution of the light Higgs boson is completely negligible. Thus the $m_H = 100$ GeV curve represents an estimate of the contributions due to W bremsstrahlung and transverse W production, which may be called an “electroweak background” to the heavy Higgs boson signal. Comparison of the light and heavy Higgs boson curves in Fig. 2 indeed shows that the signal events are produced at large average y_{gap} .

The main effect of the third parton in the final state is a slight narrowing of the average gap width from $\langle y_{gap} \rangle = 4.9$ in the lowest order calculation to $\langle y_{gap} \rangle = 4.5$ in the full $\mathcal{O}(\alpha_s)$ result (for $m_H = 800$ GeV). There are at least two reasons for this effect: the possible emission of a third jet into the region between the original two quark jets redefines the gap region and in addition the emission of a third parton outside the gap region, *i.e.* at very large rapidities, raises the center of mass energy of the event and hence leads to a kinematical reduction of the gap width. Neither effect is very large, however.

The QCD radiation of the third parton is dominated by collinear emission close to one of the two tagging jets. Because of the coherence between initial and final state radiation the emission occurs mainly between the tagging jets and the beam axes, *i.e.* outside the gap region. This effect is demonstrated in Fig. 3 where the distribution in the rapidity difference of the third (typically soft) parton and the closest tagging jet is shown,

$$\Delta\eta_{sj} = \text{sign} \cdot (\eta_{\text{soft}} - \eta_{j,\text{closest}}) . \quad (10)$$

The sign is chosen such that positive $\Delta\eta_{sj}$ corresponds to radiation outside the interval marked by the two tagging jets and negative values correspond to radiation towards the gap region. The edge of the gap region is visible as a step at $\Delta\eta_{sj} = -0.7$ which is a result of the jet separation requirement of Eq. (3). Clearly emission of the third parton outside the

gap region is preferred. This is true both for the heavy Higgs case (solid line) and for the electroweak transverse W background, simulated by the $m_H = 100$ GeV scenario (dashed line).

The resulting radiation pattern is best appreciated by choosing the center of the gap region as the origin and then normalizing the pseudorapidity of the third parton to the gap width. This is achieved by using the variable [21]

$$z = \frac{2\eta_{\text{soft}} - \eta_{j_1} - \eta_{j_2}}{|\eta_{j_1} - \eta_{j_2}| - 1.4}. \quad (11)$$

Thus $z = 0$ corresponds to the gap center while $z = \pm 1$ indicates the edges of the gap region. The resulting radiation pattern, $d\sigma/dz$, is shown in Fig. 4. The probability for radiation into the gap region is strongly suppressed both for the heavy Higgs signal and for the electroweak background. The radiation pattern which is expected for t -channel color singlet exchange is thus confirmed at $\mathcal{O}(\alpha_s)$.

IV. QCD EFFECTS ON JET-TAGGING AND CENTRAL-JET-VETOING

When trying to observe the W^+W^- decay mode of a heavy Higgs boson at a hadron collider, one needs to fight serious physics backgrounds. The production of a top-quark pair with subsequent decay $t\bar{t} \rightarrow bW^+\bar{b}W^-$ is particularly troublesome due to the large rate of this background. Of somewhat lesser importance is $q\bar{q} \rightarrow W^+W^-$ pair production [4]. Higgs boson production via weak boson fusion differs in important aspects from these background processes. Forward-jet-tagging of the quark-jet(s) off which the initial state W 's or Z 's were radiated offers a powerful tool for background suppression [2]. In addition one can use the fact that the W 's arising from top-quark decay are always accompanied by a nearby b -quark which often manifests itself as an additional hadronic jet. When searching for the leptonic decays of the produced W 's in the central rapidity region a veto on any additional central jet constitutes a powerful tool for top-background reduction.

Single forward-jet-tagging and central-jet-vetoing were analysed in Ref. [4]. The Higgs boson signal was simulated with a full $\mathcal{O}(\alpha_{\text{QED}}^4)$ Monte Carlo program. While this appears

adequate for the analysis of tagging jet distributions, the acceptance of signal events under severe central-jet-vetoing conditions might be strongly degraded by $\mathcal{O}(\alpha_s)$ QCD corrections. This question can be addressed with the tools described in Section II.

Following Ref. [4] we consider purely leptonic decays of the two W bosons and concentrate on the Higgs resonance region by imposing stringent lepton acceptance cuts,

$$|\eta_\ell| < 2, \quad p_{T\ell} > 100 \text{ GeV}, \quad \Delta p_{T\ell\ell} > 400 \text{ GeV}. \quad (12)$$

Here $\Delta p_{T\ell\ell} = |\mathbf{p}_{T\ell_1} - \mathbf{p}_{T\ell_2}|$ is the difference of the two charged lepton transverse momenta [22].

In a second step one requires the presence of at least one hadronic jet of transverse momentum

$$p_{Tj} > 40 \text{ GeV}. \quad (13)$$

The most energetic such jet is the tagging jet candidate. In Figs. 5 and 6 the pseudorapidity and transverse momentum distributions of this jet, as obtained with the full $\mathcal{O}(\alpha_s\alpha_{\text{QED}}^4)$ Monte Carlo, are shown for a $m_H = 800 \text{ GeV}$ signal and the electroweak background as defined by a $m_H = 100 \text{ GeV}$ scenario. Most of the tagging jet candidates at low $\eta_{j,\text{tag}}$ arise from transverse W bremsstrahlung and hence a stringent rapidity cut on the tagging jet is highly efficient for the heavy Higgs signal. The transverse momentum of the tagging jet in Higgs signal events is typically quite low, while the electroweak background distribution is rather flat, reflecting the dominance of W bremsstrahlung: the strong lepton p_T cut selects high p_T W -bosons which were radiated off high transverse momentum quarks. The tagging jet distributions are quite similar to the $\mathcal{O}(\alpha_{\text{QED}}^4)$ calculation which, therefore, are not shown separately. As in Ref. [4] signal events are selected by requiring the presence of a tagging jet of

$$E_{j,\text{tag}} > 1 \text{ TeV}, \quad 3 < |\eta_{j,\text{tag}}| < 5. \quad (14)$$

Because of the presence of a third colored parton in the final state the full $\mathcal{O}(\alpha_s\alpha_{\text{QED}}^4)$ calculation yields a larger probability to find an additional jet in the central region than

the corresponding result without QCD corrections. Let us define the veto jet candidate as the remaining parton, other than the tagging jet, with largest transverse momentum. The pseudorapidity distribution of this veto jet candidate is shown in Fig. 7.

In Ref. [4] a veto of any jet in the central region satisfying the conditions

$$|\eta_j(\text{veto})| < 3, \quad p_T(\text{veto}) > 30 \text{ GeV} \quad (15)$$

was found to provide adequate top background rejection while retaining most of the signal events when neglecting QCD corrections to the Higgs signal. The cross sections for the Higgs boson signal after vetoing central jets with varying minimum transverse momentum requirements are shown in Table II for both the lowest order “2 parton calculation” and the $\mathcal{O}(\alpha_s)$ “3 parton calculation”. Also given are the efficiencies of retaining the Higgs signal after central-jet-vetoing. The 100% level corresponds to the cross section difference $\sigma(m_H = 800 \text{ GeV}) - \sigma(m_H = 100 \text{ GeV})$ before rejecting events with jets of $|\eta_j| < 3$ and transverse momenta as listed in the table.

In the phase space region which is dominated by W bremsstrahlung (as simulated by the $m_H = 100 \text{ GeV}$ scenario) QCD radiation does indeed strongly affect the efficiency of a central-jet-veto. In fact this leads to a further reduction of the electroweak background compared to the Higgs boson signal. At $\mathcal{O}(\alpha_s)$ the signal acceptance of the central-jet-veto is lowered by $\approx 20\%$ and the resulting signal cross sections are typically only $\approx 15\%$ lower than before QCD corrections. Hence the conclusions of Ref. [4] remain valid when taking real emission QCD corrections into account.

Acknowledgements This research was supported in part by the University of Wisconsin Research Committee with funds granted by the Wisconsin Alumni Research Foundation, by the U. S. Department of Energy under contract No. DE-AC02-76ER00881, and by the Texas National Research Laboratory Commission under Grants No. RGFY9273 and FCFY9212.

APPENDIX A: MATRIX ELEMENTS

The external state of the processes considered in Section II consists of four quarks, one gluon, a W^+ and a W^- boson. The W^\pm bosons will be taken later to decay into leptons, but this does not change the nature of the calculation. The four (anti)quarks are labelled as a, b, c, d , along with their corresponding momenta p_a, p_b, p_c, p_d , and helicities $\lambda_a, \lambda_b, \lambda_c, \lambda_d$. The four (anti)quarks are paired to form two fermion lines, denoted as (ac) for fermion flow from $a \rightarrow c$, and (bd) for fermion flow from $b \rightarrow d$. The gluon is taken to have a four-momentum given by p_e , and helicity λ_e . The momenta of the W^+ and W^- final-state bosons are denoted by q_1 and q_2 , respectively.

The $q\bar{q}q\bar{q}W^+W^-g$ amplitudes are evaluated numerically using the HELAS program package [8]. The HELAS program contains subroutines evaluating and multiplying the various factors in the Feynman graphs. Hence we shall employ a notation directly relating to the structure of HELAS. To begin, the generalized propagator for a vector boson of mass M in the unitary gauge is given by

$$D^{\mu\nu}(q^2, M) = \frac{-i}{q^2 - M^2 + iM\Gamma \Theta(q^2)} \left[g^{\mu\nu} - \frac{q^\mu q^\nu}{M^2} \right] \quad (\text{A1})$$

with q^2 representing the momentum transfer squared, and Γ denoting the q^2 independent decay width of the intermediate particle. The step function $\Theta(q^2)$ eliminates the imaginary part of the vector boson propagator for spacelike momentum transfer. The analogous choice for the heavy Higgs boson propagator will introduce only a small error compared to unitarity requirements [11]. Similarly, for massless particles, the propagator function is defined as

$$d^{\mu\nu}(q^2) = -\frac{i}{q^2} g^{\mu\nu} \quad (\text{A2})$$

Vertex insertions are defined via

$$V_i^\mu = \gamma^\mu \left[g_V^i + g_A^i \gamma^5 \right] \quad (\text{A3})$$

where the index i on the vector and axial coupling constants g_V^i and g_A^i will list the vector bosons and fermions coupling at a particular vertex.

The zero-width-approximation is employed in order to include spin-correlation effects of the W^\pm decay products. The polarization vectors of the final state W bosons are denoted by $\epsilon_1^*(q_1)$ for the W^+ boson and $\epsilon_2^*(q_2)$ for the W^- boson.

$$\epsilon_1^\mu(q_1, \lambda_1)^* = J_{12}^\mu(k_1, k_2, \rho_1, \rho_2) \sqrt{\frac{\pi}{M_W \Gamma_W}} \quad (\text{A4})$$

$$\epsilon_2^\mu(q_2, \lambda_2)^* = J_{34}^\mu(k_3, k_4, \rho_3, \rho_4) \sqrt{\frac{\pi}{M_W \Gamma_W}} \quad (\text{A5})$$

where the truncated decay current is defined in terms of the final state fermion spinors

$$J_{12}^\mu = \bar{u}(k_1, \rho_1) V_{Wff}^\mu v(k_2, \rho_2) \quad (\text{A6})$$

$$J_{34}^\mu = \bar{u}(k_3, \rho_3) V_{Wff}^\mu v(k_4, \rho_4) \quad (\text{A7})$$

Inserting these decay currents for the W polarization vectors the resulting matrix elements will describe the full process

$$q_a q_c \rightarrow q_b q_d W^+ W^- g, \quad W^+ \rightarrow \ell_1 \bar{\ell}_2, \quad W^- \rightarrow \ell_3 \bar{\ell}_4, \quad (\text{A8})$$

and all processes related by crossing of the quarks and gluons.

In order to simplify the spinor algebra we use a bra and ket notation:

$$u(p_a, \lambda_a) = |a\rangle \quad (\text{A9})$$

$$u(p_b, \lambda_b) = |b\rangle \quad (\text{A10})$$

$$\bar{u}(p_c, \lambda_c) = \langle c| \quad (\text{A11})$$

$$\bar{u}(p_d, \lambda_d) = \langle d| \quad (\text{A12})$$

and similarly, the wavefunctions for antiquarks are defined as

$$\bar{v}(p_a, -\lambda_a) = \langle a| \quad (\text{A13})$$

$$\bar{v}(p_b, -\lambda_b) = \langle b| \quad (\text{A14})$$

$$v(p_c, -\lambda_c) = |c\rangle \quad (\text{A15})$$

$$v(p_d, -\lambda_d) = |d\rangle \quad (\text{A16})$$

The currents, corresponding to the splitting of a virtual γ, Z into a final-state W^+W^- pair via the triple-boson vertex, are

$$U_\gamma^\mu = d^{\mu\nu}((q_1 + q_2)^2)E_{\rho\lambda\nu}\epsilon_1^{\lambda*}\epsilon_2^{\rho*} \quad (\text{A17})$$

$$U_Z^\mu = D^{\mu\nu}((q_1 + q_2)^2, M_Z)F_{\rho\lambda\nu}\epsilon_1^{\lambda*}\epsilon_2^{\rho*} \quad (\text{A18})$$

where E represents the $WW\gamma$ triple-boson vertex rule, with the index ordering corresponding to incoming $W^+W^-\gamma$ bosons or outgoing $W^-W^+\gamma$ bosons. The tensor F represents the WWZ triple-boson vertex rule in analogous notation.

Off-shell fermion wavefunctions, corresponding to gauge boson emission off the fermion lines, are defined via

$$|1, a\rangle = \frac{i}{\not{p}_a - \not{q}_1}\epsilon_1^{\mu*}V_\mu^{Wff}|a\rangle \quad (\text{A19})$$

$$|2, 1, a\rangle = \frac{i}{\not{p}_a - \not{q}_1 - \not{q}_2}\epsilon_2^{\mu*}V_\mu^{Wff}|1, a\rangle \quad (\text{A20})$$

$$|U, a\rangle = \frac{i}{\not{p}_a - \not{q}_1 - \not{q}_2}\left(U_\gamma^\mu V_\mu^{\gamma ff} + U_Z^\mu V_\mu^{Zff}\right)|a\rangle \quad (\text{A21})$$

$$\langle c, 2| = \langle c|V_\mu^{Wff}\epsilon_2^{\mu*}\frac{i}{\not{p}_c + \not{q}_2} \quad (\text{A22})$$

$$\langle c, 2, 1| = \langle c, 2|V_\mu^{Wff}\epsilon_1^{\mu*}\frac{i}{\not{p}_c + \not{q}_2 + \not{q}_1} \quad (\text{A23})$$

$$\langle c, U| = \langle c|\left(U_\gamma^\mu V_\mu^{\gamma ff} + U_Z^\mu V_\mu^{Zff}\right)\frac{i}{\not{p}_c + \not{q}_2 + \not{q}_1} \quad (\text{A24})$$

Similar expressions hold for wavefunctions involving fermions b and d .

Gluon insertions along a fermion line are notated as

$$|g, a\rangle = \frac{i}{\not{p}_a - \not{p}_e}\epsilon_g^{\mu*}V_\mu^{gff}|a\rangle \quad (\text{A25})$$

$$|1, g, a\rangle = \frac{i}{\not{p}_a - \not{p}_e - \not{q}_1}\epsilon_1^{\mu*}V_\mu^{Wff}|g, a\rangle \quad (\text{A26})$$

$$|g, 1, a\rangle = \frac{i}{\not{p}_a - \not{p}_e - \not{q}_1}\epsilon_g^{\mu*}V_\mu^{gff}|1, a\rangle \quad (\text{A27})$$

$$|2, g, 1, a\rangle = \frac{i}{\not{p}_a - \not{p}_e - \not{q}_1 - \not{q}_2}\epsilon_2^{\mu*}V_\mu^{Wff}|g, 1, a\rangle \quad (\text{A28})$$

$$|g, 2, 1, a\rangle = \frac{i}{\not{p}_a - \not{p}_e - \not{q}_1 - \not{q}_2}\epsilon_g^{\mu*}V_\mu^{gff}|2, 1, a\rangle \quad (\text{A29})$$

$$\langle c, g| = \langle c|V_\mu^{gff}\epsilon_g^{\mu*}\frac{i}{\not{p}_c + \not{p}_e} \quad (\text{A30})$$

$$\langle c, g, 2 | = \langle c, g | V_\mu^{Wff} \epsilon_2^{\mu*} \frac{i}{\not{p}_c + \not{p}_e + \not{q}_2} \quad (\text{A31})$$

$$\langle c, 2, g | = \langle c, 2 | V_\mu^{gff} \epsilon_g^{\mu*} \frac{i}{\not{p}_c + \not{p}_e + \not{q}_2} \quad (\text{A32})$$

$$\langle c, 2, g, 1 | = \langle c, 2, g | V_\mu^{Wff} \epsilon_1^{\mu*} \frac{i}{\not{p}_c + \not{p}_e + \not{q}_1 + \not{q}_2} \quad (\text{A33})$$

$$\langle c, 2, 1, g | = \langle c, 2, 1 | V_\mu^{gff} \epsilon_g^{\mu*} \frac{i}{\not{p}_c + \not{p}_e + \not{q}_1 + \not{q}_2} \quad (\text{A34})$$

Simple electroweak currents are denoted as in

$$J_\gamma^\mu(ac) = d^{\mu\nu}((p_a - p_c)^2) \langle c | V_\nu^{\gamma ff} | a \rangle \quad (\text{A35})$$

$$J_W^\mu(ac) = D^{\mu\nu}((p_a - p_c)^2, M_W) \langle c | V_\nu^{Wff} | a \rangle \quad (\text{A36})$$

$$J_Z^\mu(ac) = D^{\mu\nu}((p_a - p_c)^2, M_Z) \langle c | V_\nu^{Zff} | a \rangle \quad (\text{A37})$$

$$J_3^\mu(ac) = \cos \theta_W J_Z^\mu(ac) + \sin \theta_W J_\gamma^\mu(ac) \quad (\text{A38})$$

with (ac) representing fermion current flow from $a \rightarrow c$. Fermion current flow from $c \rightarrow a$ would be represented by the argument (ca) .

When including gluon emission the notation

$$J_{g\gamma}^\mu(ac) = d^{\mu\nu}((p_a - p_c - p_e)^2) \langle c | V_\nu^{\gamma ff} | g, a \rangle \quad (\text{A39})$$

$$J_{\gamma g}^\mu(ac) = d^{\mu\nu}((p_a - p_c - p_e)^2) \langle c, g | V_\nu^{\gamma ff} | a \rangle \quad (\text{A40})$$

$$J_{g\gamma}^\mu(ca) = d^{\mu\nu}((p_c - p_a - p_e)^2) \langle a, g | V_\nu^{\gamma ff} | c \rangle \quad (\text{A41})$$

$$J_{\gamma g}^\mu(ca) = d^{\mu\nu}((p_c - p_a - p_e)^2) \langle a | V_\nu^{\gamma ff} | g, c \rangle \quad (\text{A42})$$

is used, and similarly more complicated single W boson emission currents are denoted by

$$J_{1\gamma}^\mu(ac) = d^{\mu\nu}((p_a - p_c - q_1)^2) \langle c | V_\nu^{\gamma ff} | 1, a \rangle \quad (\text{A43})$$

$$J_{1W}^\mu(ac) = D^{\mu\nu}((p_a - p_c - q_1)^2, M_W) \langle c | V_\nu^{Wff} | 1, a \rangle \quad (\text{A44})$$

$$J_{Z1}^\mu(ac) = D^{\mu\nu}((p_a - p_c - q_1)^2, M_Z) \langle c, 1 | V_\nu^{Zff} | a \rangle . \quad (\text{A45})$$

Including the emission of a gluon, the notation of the latter three changes to

$$J_{g\gamma 1}^\mu(ac) = d^{\mu\nu}((p_a - p_c - p_e - q_1)^2) \langle c, 1 | V_\nu^{\gamma ff} | g, a \rangle \quad (\text{A46})$$

$$J_{Wg1}^\mu(ac) = D^{\mu\nu}((p_a - p_c - p_e - q_1)^2, M_W)\langle c, 1, g|V_\nu^{Wff}|a\rangle \quad (\text{A47})$$

$$J_{Z1g}^\mu(ac) = D^{\mu\nu}((p_a - p_c - p_e - q_1)^2, M_Z)\langle c, g, 1|V_\nu^{Zff}|a\rangle \quad (\text{A48})$$

and similarly for interchange of outgoing bosons 1 and 2, interchange of fermion current flow $a \leftrightarrow c$, interchange of fermion line (ac) for (bd) , or a combination of any and/or all of the above interchanges. Notice that in all cases the space-time index of the current corresponds to the *explicitly* listed *electroweak* boson in the index identifying the current.

Double W boson emission currents may be defined similarly, as in the examples

$$J_{12\gamma}^\mu(ac) = d^{\mu\nu}((p_a - p_c - q_1 - q_2)^2)\langle c|V_\nu^{\gamma ff}|2, 1, a\rangle \quad (\text{A49})$$

$$J_{1W2}^\mu(ac) = D^{\mu\nu}((p_a - p_c - q_1 - q_2)^2, M_W)\langle c, 2|V_\nu^{Wff}|1, a\rangle \quad (\text{A50})$$

$$J_{ZU}^\mu(ac) = D^{\mu\nu}((p_a - p_c - q_1 - q_2)^2, M_Z)\langle c, U|V_\nu^{Zff}|a\rangle . \quad (\text{A51})$$

Including gluon emission another index needs to be added,

$$J_{1g\gamma 2}^\mu(ac) = d^{\mu\nu}((p_a - p_c - p_e - q_1 - q_2)^2)\langle c, 2|V_\nu^{\gamma ff}|g, 1, a\rangle \quad (\text{A52})$$

$$J_{WgU}^\mu(ac) = D^{\mu\nu}((p_a - p_c - p_e - q_1 - q_2)^2, M_W)\langle c, U, g|V_\nu^{Wff}|a\rangle \quad (\text{A53})$$

$$J_{gZ12}^\mu(ac) = D^{\mu\nu}((p_a - p_c - p_e - q_1 - q_2)^2, M_Z)\langle c, 2, 1|V_\nu^{Zff}|g, a\rangle , \quad (\text{A54})$$

where again, all possible interchanges of outgoing bosons, fermion current flows, and fermion lines are allowed.

For sums of currents involving gluon emission off the same fermion line, a semi-colon notation is introduced. For example,

$$J_{\gamma;g}^\mu(ac) = J_{g\gamma}^\mu(ac) + J_{\gamma g}^\mu(ac) \quad (\text{A55})$$

$$J_{Z12;g}^\mu(ac) = J_{gZ12}^\mu(ac) + J_{Zg12}^\mu(ac) + J_{Z1g2}^\mu(ac) + J_{Z12g}^\mu(ac) \quad (\text{A56})$$

represent a photon and a Z current given by the sum of currents involving a gluon emission along *all* possible topologically distinct locations on the fermion line. In terms of the bra and ket notation, the semi-colon notation is analogously introduced by example,

$$\begin{aligned} \langle c, 1, 2|X|a\rangle_{;g} &= \langle c, 1, 2|X|g, a\rangle + \langle c, 1, 2, g|X|a\rangle \\ &+ \langle c, 1, g, 2|X|a\rangle + \langle c, g, 1, 2|X|a\rangle, \end{aligned} \quad (\text{A57})$$

where X is an arbitrary vertex insertion.

The scalar current obtained from WW fusion into a Higgs boson is defined via

$$H_{\mu\nu}^{WWH} = D((q_1 + q_2)^2, M_H)I_{\mu\nu}^{WWH} \quad (\text{A58})$$

where $I_{\mu\nu}^{WWH}$ represents the WWH vertex rule. Similarly, $I_{\mu\nu}^{ZZH}$ represents the ZZH vertex rule.

The $SU(2)$ quadruple-boson vertices are represented by S and T . $S_{\mu\nu\lambda\rho}$ represents the $WWWW$ effective coupling, which includes the contact term, as well as s -channel and t -channel γ, Z exchange terms. $T_{\mu\nu\lambda\rho}$ represents the WW^3WW^3 effective coupling, which includes the contact term, as well as t -channel and u -channel W^\pm exchange terms.

The tensor G represents the WWW^3 triple-boson vertex rule, with the index ordering corresponding to incoming $W^+W^-W^3$ bosons, or outgoing $W^-W^+W^3$ bosons, respectively. The current J_3 is, as defined in Eq. (A38), a $SU(2)$ superposition of γ, Z currents.

With this notation we can now express the amplitudes, which correspond to the various Feynman graphs, in a very compact notation which can directly be translated into a calling sequence for HELAS subroutines. For the Feynman graphs of Figure 8.a one gets

$$-i\mathcal{M}_1(a) = J_{W;g}^\mu(ac)J_W^\nu(bd)I_{\mu\nu}^{WWH}H_{\lambda\rho}^{WWH}\epsilon_1^{\lambda*}\epsilon_2^{\rho*} \quad (\text{A59})$$

$$-i\mathcal{M}_1(b) = J_{W;g}^\nu(bd)J_W^\mu(ac)I_{\mu\nu}^{WWH}H_{\lambda\rho}^{WWH}\epsilon_1^{\lambda*}\epsilon_2^{\rho*} \quad (\text{A60})$$

where $\mathcal{M}(a)$ represents an amplitude including all distinguishable gluon emission insertions along the fermion line $a \rightarrow c$. Similarly, $\mathcal{M}(b)$ represents an amplitude including all distinguishable gluon emission insertions along the fermion line $b \rightarrow d$.

Only the $\mathcal{M}(a)$ amplitudes are shown below, with the $\mathcal{M}(b)$ amplitudes derived via interchange of the fermion indices ($ac \rightarrow bd$). The remaining $\mathcal{M}(a)$ amplitudes can be represented as follows

$$-i\mathcal{M}_2(a) = J_{W;g}^\mu(ac)J_W^\nu(bd)I_{\mu\lambda}^{WWH}H_{\nu\rho}^{WWH}\epsilon_1^{\lambda*}\epsilon_2^{\rho*} \quad (\text{A61})$$

$$-i\mathcal{M}_3(a) = J_{W;g}^\mu(ac)J_W^\nu(bd)I_{\mu\rho}^{WWH}H_{\nu\lambda}^{WWH}\epsilon_1^{\lambda*}\epsilon_2^{\rho*} \quad (\text{A62})$$

with corresponding Feynman diagrams presented in Figure 8.b. Notice that for a given set of external quark flavors only one of the two amplitudes \mathcal{M}_2 or \mathcal{M}_3 will be nonvanishing: \mathcal{M}_2 corresponds to a W^+ coupling to the (ac) quark line while for \mathcal{M}_3 the emission of a W^- off the (ac) quark line must be allowed. Analogous flavor selection rules will be implied for all remaining diagrams as well. The amplitudes for these are given by

$$-i\mathcal{M}_4(a) = J_{W;g}^\mu(ac)J_W^\nu(bd)S_{\mu\nu\rho\lambda}\epsilon_1^{\lambda*}\epsilon_2^{\rho*} \quad (\text{A63})$$

$$-i\mathcal{M}_5(a) = J_{W;g}^\mu(ac)J_W^\nu(bd)S_{\nu\mu\rho\lambda}\epsilon_1^{\lambda*}\epsilon_2^{\rho*} \quad (\text{A64})$$

$$-i\mathcal{M}_6(a) = J_{Z;g}^\mu(ac)J_Z^\nu(bd)I_{\mu\nu}^{ZZH}H_{\lambda\rho}^{WWH}\epsilon_1^{\lambda*}\epsilon_2^{\rho*} \quad (\text{A65})$$

$$-i\mathcal{M}_7(a) = J_{3;g}^\mu(ac)J_3^\nu(bd)T_{\rho\mu\lambda\nu}\epsilon_1^{\lambda*}\epsilon_2^{\rho*} \quad (\text{A66})$$

with corresponding Feynman diagrams presented in Figure 9

$$-i\mathcal{M}_8(a) = J_{2W;g}^\mu(ac)J_3^\nu(bd)G_{\mu\lambda\nu}\epsilon_1^{\lambda*} \quad (\text{A67})$$

$$-i\mathcal{M}_9(a) = J_{W2;g}^\mu(ac)J_3^\nu(bd)G_{\mu\lambda\nu}\epsilon_1^{\lambda*} \quad (\text{A68})$$

$$-i\mathcal{M}_{10}(a) = J_{1W;g}^\mu(ac)J_3^\nu(bd)G_{\lambda\mu\nu}\epsilon_2^{\lambda*} \quad (\text{A69})$$

$$-i\mathcal{M}_{11}(a) = J_{W1;g}^\mu(ac)J_3^\nu(bd)G_{\lambda\mu\nu}\epsilon_2^{\lambda*} \quad (\text{A70})$$

$$-i\mathcal{M}_{12}(a) = J_{3;g}^\mu(ac)J_{2W}^\nu(bd)G_{\nu\lambda\mu}\epsilon_1^{\lambda*} \quad (\text{A71})$$

$$-i\mathcal{M}_{13}(a) = J_{3;g}^\mu(ac)J_{W2}^\nu(bd)G_{\nu\lambda\mu}\epsilon_1^{\lambda*} \quad (\text{A72})$$

$$-i\mathcal{M}_{14}(a) = J_{3;g}^\mu(ac)J_{1W}^\nu(bd)G_{\lambda\nu\mu}\epsilon_2^{\lambda*} \quad (\text{A73})$$

$$-i\mathcal{M}_{15}(a) = J_{3;g}^\mu(ac)J_{W1}^\nu(bd)G_{\lambda\nu\mu}\epsilon_2^{\lambda*} \quad (\text{A74})$$

$$-i\mathcal{M}_{16}(a) = J_{W;g}^\mu(ac)J_{23}^\nu(bd)G_{\mu\lambda\nu}\epsilon_1^{\lambda*} \quad (\text{A75})$$

$$-i\mathcal{M}_{17}(a) = J_{W;g}^\mu(ac)J_{32}^\nu(bd)G_{\mu\lambda\nu}\epsilon_1^{\lambda*} \quad (\text{A76})$$

$$-i\mathcal{M}_{18}(a) = J_{W;g}^\mu(ac)J_{13}^\nu(bd)G_{\lambda\mu\nu}\epsilon_2^{\lambda*} \quad (\text{A77})$$

$$-i\mathcal{M}_{19}(a) = J_{W;g}^\mu(ac)J_{31}^\nu(bd)G_{\lambda\mu\nu}\epsilon_2^{\lambda*} \quad (\text{A78})$$

$$-i\mathcal{M}_{20}(a) = J_{23;g}^\mu(ac)J_W^\nu(bd)G_{\nu\lambda\mu}\epsilon_1^{\lambda*} \quad (\text{A79})$$

$$-i\mathcal{M}_{21}(a) = J_{32;g}^\mu(ac)J_W^\nu(bd)G_{\nu\lambda\mu}\epsilon_1^{\lambda*} \quad (\text{A80})$$

$$-i\mathcal{M}_{22}(a) = J_{13;g}^\mu(ac)J_W^\nu(bd)G_{\lambda\nu\mu}\epsilon_2^{\lambda*} \quad (\text{A81})$$

$$-i\mathcal{M}_{23}(a) = J_{31;g}^\mu(ac)J_W^\nu(bd)G_{\lambda\nu\mu}\epsilon_2^{\lambda*} \quad (\text{A82})$$

$$-i\mathcal{M}_{24}(a) = J_{12\gamma;g}^\mu(ac)\langle d|V_\mu^{\gamma ff}|b\rangle + J_{12Z;g}^\mu(ac)\langle d|V_\mu^{Zff}|b\rangle \quad (\text{A83})$$

$$-i\mathcal{M}_{25}(a) = J_{1\gamma 2;g}^\mu(ac)\langle d|V_\mu^{\gamma ff}|b\rangle + J_{1Z 2;g}^\mu(ac)\langle d|V_\mu^{Zff}|b\rangle \quad (\text{A84})$$

$$-i\mathcal{M}_{26}(a) = J_{\gamma 12;g}^\mu(ac)\langle d|V_\mu^{\gamma ff}|b\rangle + J_{Z1 2;g}^\mu(ac)\langle d|V_\mu^{Zff}|b\rangle \quad (\text{A85})$$

$$-i\mathcal{M}_{27}(a) = J_{21\gamma;g}^\mu(ac)\langle d|V_\mu^{\gamma ff}|b\rangle + J_{21Z;g}^\mu(ac)\langle d|V_\mu^{Zff}|b\rangle \quad (\text{A86})$$

$$-i\mathcal{M}_{28}(a) = J_{2\gamma 1;g}^\mu(ac)\langle d|V_\mu^{\gamma ff}|b\rangle + J_{2Z 1;g}^\mu(ac)\langle d|V_\mu^{Zff}|b\rangle \quad (\text{A87})$$

$$-i\mathcal{M}_{29}(a) = J_{\gamma 21;g}^\mu(ac)\langle d|V_\mu^{\gamma ff}|b\rangle + J_{Z2 1;g}^\mu(ac)\langle d|V_\mu^{Zff}|b\rangle \quad (\text{A88})$$

$$-i\mathcal{M}_{30}(a) = J_{12\gamma}^\mu(bd)\langle c|V_\mu^{\gamma ff}|a\rangle_{;g} + J_{12Z}^\mu(bd)\langle c|V_\mu^{Zff}|a\rangle_{;g} \quad (\text{A89})$$

$$-i\mathcal{M}_{31}(a) = J_{1\gamma 2}^\mu(bd)\langle c|V_\mu^{\gamma ff}|a\rangle_{;g} + J_{1Z 2}^\mu(bd)\langle c|V_\mu^{Zff}|a\rangle_{;g} \quad (\text{A90})$$

$$-i\mathcal{M}_{32}(a) = J_{\gamma 12}^\mu(bd)\langle c|V_\mu^{\gamma ff}|a\rangle_{;g} + J_{Z1 2}^\mu(bd)\langle c|V_\mu^{Zff}|a\rangle_{;g} \quad (\text{A91})$$

$$-i\mathcal{M}_{33}(a) = J_{21\gamma}^\mu(bd)\langle c|V_\mu^{\gamma ff}|a\rangle_{;g} + J_{21Z}^\mu(bd)\langle c|V_\mu^{Zff}|a\rangle_{;g} \quad (\text{A92})$$

$$-i\mathcal{M}_{34}(a) = J_{2\gamma 1}^\mu(bd)\langle c|V_\mu^{\gamma ff}|a\rangle_{;g} + J_{2Z 1}^\mu(bd)\langle c|V_\mu^{Zff}|a\rangle_{;g} \quad (\text{A93})$$

$$-i\mathcal{M}_{35}(a) = J_{\gamma 21}^\mu(bd)\langle c|V_\mu^{\gamma ff}|a\rangle_{;g} + J_{Z2 1}^\mu(bd)\langle c|V_\mu^{Zff}|a\rangle_{;g} \quad (\text{A94})$$

with corresponding Feynman diagrams presented in Figure 10

$$-i\mathcal{M}_{36}(a) = J_{1\gamma;g}^\mu(ac)\langle d|V_\mu^{\gamma ff}|2,b\rangle + J_{1Z;g}^\mu(ac)\langle d|V_\mu^{Zff}|2,b\rangle \quad (\text{A95})$$

$$-i\mathcal{M}_{37}(a) = J_{\gamma 1;g}^\mu(ac)\langle d|V_\mu^{\gamma ff}|2,b\rangle + J_{Z1;g}^\mu(ac)\langle d|V_\mu^{Zff}|2,b\rangle \quad (\text{A96})$$

$$-i\mathcal{M}_{38}(a) = J_{1\gamma;g}^\mu(ac)\langle d, 2|V_\mu^{\gamma ff}|b\rangle + J_{1Z;g}^\mu(ac)\langle d, 2|V_\mu^{Zff}|b\rangle \quad (\text{A97})$$

$$-i\mathcal{M}_{39}(a) = J_{\gamma 1;g}^\mu(ac)\langle d, 2|V_\mu^{\gamma ff}|b\rangle + J_{Z1;g}^\mu(ac)\langle d, 2|V_\mu^{Zff}|b\rangle \quad (\text{A98})$$

$$-i\mathcal{M}_{40}(a) = J_{2\gamma;g}^\mu(ac)\langle d|V_\mu^{\gamma ff}|1,b\rangle + J_{2Z;g}^\mu(ac)\langle d|V_\mu^{Zff}|1,b\rangle \quad (\text{A99})$$

$$-i\mathcal{M}_{41}(a) = J_{\gamma 2;g}^\mu(ac)\langle d|V_\mu^{\gamma ff}|1,b\rangle + J_{Z2;g}^\mu(ac)\langle d|V_\mu^{Zff}|1,b\rangle \quad (\text{A100})$$

$$-i\mathcal{M}_{42}(a) = J_{2\gamma;g}^\mu(ac)\langle d, 1|V_\mu^{\gamma ff}|b\rangle + J_{2Z;g}^\mu(ac)\langle d, 1|V_\mu^{Zff}|b\rangle \quad (\text{A101})$$

$$-i\mathcal{M}_{43}(a) = J_{\gamma 2;g}^\mu(ac)\langle d, 1|V_\mu^{\gamma ff}|b\rangle + J_{Z2;g}^\mu(ac)\langle d, 1|V_\mu^{Zff}|b\rangle \quad (\text{A102})$$

$$-i\mathcal{M}_{44}(a) = J_{U\gamma;g}^\mu(ac)\langle d|V^{\gamma ff}|b\rangle + J_{UZ;g}^\mu(ac)\langle d|V^{Zff}|b\rangle \quad (\text{A103})$$

$$-i\mathcal{M}_{45}(a) = J_{\gamma U;g}^\mu(ac)\langle d|V^{\gamma ff}|b\rangle + J_{ZU;g}^\mu(ac)\langle d|V^{Zff}|b\rangle \quad (\text{A104})$$

$$-i\mathcal{M}_{46}(a) = J_{U\gamma}^\mu(bd)\langle c|V^{\gamma ff}|a\rangle_{;g} + J_{UZ}^\mu(bd)\langle c|V^{Zff}|a\rangle_{;g} \quad (\text{A105})$$

$$-i\mathcal{M}_{47}(a) = J_{\gamma U}^\mu(bd)\langle c|V^{\gamma ff}|a\rangle_{;g} + J_{ZU}^\mu(bd)\langle c|V^{Zff}|a\rangle_{;g} \quad (\text{A106})$$

$$-i\mathcal{M}_{48}(a) = J_{12W;g}^\mu(ac)\langle d|V_\mu^{Wff}|b\rangle \quad (\text{A107})$$

$$-i\mathcal{M}_{49}(a) = J_{21W;g}^\mu(ac)\langle d|V_\mu^{Wff}|b\rangle \quad (\text{A108})$$

$$-i\mathcal{M}_{50}(a) = J_{W21;g}^\mu(ac)\langle d|V_\mu^{Wff}|b\rangle \quad (\text{A109})$$

$$-i\mathcal{M}_{51}(a) = J_{W12;g}^\mu(ac)\langle d|V_\mu^{Wff}|b\rangle \quad (\text{A110})$$

$$-i\mathcal{M}_{52}(a) = J_{21W}^\mu(bd)\langle c|V_\mu^{Wff}|a\rangle_{;g} \quad (\text{A111})$$

$$-i\mathcal{M}_{53}(a) = J_{12W}^\mu(bd)\langle c|V_\mu^{Wff}|a\rangle_{;g} \quad (\text{A112})$$

$$-i\mathcal{M}_{54}(a) = J_{W12}^\mu(bd)\langle c|V_\mu^{Wff}|a\rangle_{;g} \quad (\text{A113})$$

$$-i\mathcal{M}_{55}(a) = J_{W21}^\mu(bd)\langle c|V_\mu^{Wff}|a\rangle_{;g} \quad (\text{A114})$$

with corresponding Feynman diagrams presented in Figure 11, and finally

$$-i\mathcal{M}_{56}(a) = J_{2W;g}^\mu(ac)\langle d|V_\mu^{Wff}|1, b\rangle \quad (\text{A115})$$

$$-i\mathcal{M}_{57}(a) = J_{W2;g}^\mu(ac)\langle d|V_\mu^{Wff}|1, b\rangle \quad (\text{A116})$$

$$-i\mathcal{M}_{58}(a) = J_{2W;g}^\mu(ac)\langle d, 1|V_\mu^{Wff}|b\rangle \quad (\text{A117})$$

$$-i\mathcal{M}_{59}(a) = J_{W2;g}^\mu(ac)\langle d, 1|V_\mu^{Wff}|b\rangle \quad (\text{A118})$$

$$-i\mathcal{M}_{60}(a) = J_{1W;g}^\mu(ac)\langle d|V_\mu^{Wff}|2, b\rangle \quad (\text{A119})$$

$$-i\mathcal{M}_{61}(a) = J_{W1;g}^\mu(ac)\langle d|V_\mu^{Wff}|2, b\rangle \quad (\text{A120})$$

$$-i\mathcal{M}_{62}(a) = J_{1W;g}^\mu(ac)\langle d, 2|V_\mu^{Wff}|b\rangle \quad (\text{A121})$$

$$-i\mathcal{M}_{63}(a) = J_{W1;g}^\mu(ac)\langle d, 2|V_\mu^{Wff}|b\rangle \quad (\text{A122})$$

$$-i\mathcal{M}_{64}(a) = J_{UW;g}^\mu(ac)\langle d|V^{Wff}|b\rangle \quad (\text{A123})$$

$$-i\mathcal{M}_{65}(a) = J_{WU;g}^\mu(ac)\langle d|V^{Wff}|b\rangle \quad (\text{A124})$$

$$-i\mathcal{M}_{66}(a) = J_{UW}^\mu(bd)\langle c|V^{Wff}|a\rangle_{;g} \quad (\text{A125})$$

$$-i\mathcal{M}_{67}(a) = J_{WU}^\mu(bd)\langle c|V^{Wff}|a\rangle_{;g} \quad (\text{A126})$$

with corresponding Feynman diagrams presented in Figure 12. Notice that there are no

diagrams involving Goldstone bosons. This is a remnant of the choice of the unitary gauge for this calculation.

Once the individual amplitudes are evaluated, the two amplitude sums are calculated as

$$\mathcal{M}(a) = \mathcal{M}_1(a) + \mathcal{M}_2(a) + \dots + \mathcal{M}_{67}(a) \quad (\text{A127})$$

$$\mathcal{M}(b) = \mathcal{M}_1(b) + \mathcal{M}_2(b) + \dots + \mathcal{M}_{67}(b) \quad (\text{A128})$$

The overall amplitude including the QCD color structure is hence

$$\mathcal{M} = T_{ac}^i \delta_{bd} \mathcal{M}(a) + \delta_{ac} T_{bd}^i \mathcal{M}(b) \quad (\text{A129})$$

where a, b, c and d represent the color indices of the four quarks, and i represents the color index of the attached gluon. The required sum of the amplitude square, $|\mathcal{M}|^2$, over all external colors thus yields

$$\sum_{\text{colors}} |\mathcal{M}|^2 = N \frac{N^2 - 1}{2} \left(|\mathcal{M}(a)|^2 + |\mathcal{M}(b)|^2 \right) \quad (\text{A130})$$

for an $SU(N)$ gauge theory ($N = 3$ for QCD).

When identical final-state fermions are present one must anti-symmetrize the resulting matrix element. This complicates the resulting color structure. In comparison with Eqn. A129 above, the resulting amplitude contains both t and u -channel processes as

$$\begin{aligned} \mathcal{M} &= T_{ac}^i \delta_{bd} \mathcal{M}(a) + \delta_{ac} T_{bd}^i \mathcal{M}(b) \\ &\quad - T_{ad}^i \delta_{bc} \mathcal{M}(a)[c \leftrightarrow d] - \delta_{ad} T_{bc}^i \mathcal{M}(b)[c \leftrightarrow d] \end{aligned} \quad (\text{A131})$$

This leads to modified terms in the analogue of Eq. (A130). Defining

$$\mathcal{M}'_1 = \mathcal{M}(a) + \mathcal{M}(b) - \mathcal{M}(a)[c \leftrightarrow d] - \mathcal{M}(b)[c \leftrightarrow d] \quad (\text{A132})$$

$$\mathcal{M}'_2 = \mathcal{M}(a) - \mathcal{M}(b) \quad (\text{A133})$$

$$\mathcal{M}'_3 = \mathcal{M}(a)[c \leftrightarrow d] - \mathcal{M}(b)[c \leftrightarrow d] \quad (\text{A134})$$

$$\mathcal{M}'_4 = \mathcal{M}(a) + \mathcal{M}(b) + \mathcal{M}(a)[c \leftrightarrow d] + \mathcal{M}(b)[c \leftrightarrow d] \quad (\text{A135})$$

one obtains

$$\sum_{\text{colors}} |\mathcal{M}|^2 = \sum_{j=1}^4 C'_j |\mathcal{M}'_j|^2 \quad (\text{A136})$$

with

$$C'_1 = (N + 2) \left(\frac{N^2 - 1}{2} \right) \quad (\text{A137})$$

$$C'_2 = N \left(\frac{N^2 - 1}{2} \right) \quad (\text{A138})$$

$$C'_3 = N \left(\frac{N^2 - 1}{2} \right) \quad (\text{A139})$$

$$C'_4 = (N - 2) \left(\frac{N^2 - 1}{2} \right) . \quad (\text{A140})$$

Within $SU(3)$ one needs to insert the color factors $C'_1 = 20$, $C'_2 = C'_3 = 12$ and $C'_4 = 4$. Inclusion of s -channel diagrams, and possible t and s -channel interference proceeds with identical color structures as for the t -channel, and t and u -channel interference cases, respectively.

REFERENCES

- [1] J. Bagger *et al.*, preprint FERMILAB-PUB-93-040-T (1993).
- [2] R. Kleiss and W. J. Stirling, *Phys. Lett.* **B200**, 193 (1988); D. Froideveaux, Proceedings of the LHC Workshop (1990), CERN 90-10, Vol II, p. 444; M. H. Seymour, *ibid*, p. 557.
- [3] V. Barger *et al.*, *Phys. Rev.* **D44**, 1426 (1991).
- [4] V. Barger, K. Cheung, T. Han, and D. Zeppenfeld, *Phys. Rev.* **D44**, 2701 (1991); preprint MAD/PH/757 (1993).
- [5] J. F. Gunion *et al.*, *Phys. Rev.* **D40**, 2223 (1989).
- [6] Y. L. Dokshitzer, V. A. Khoze, and S. Troyan, in *Proceedings of the 6th International Conference on Physics in Collisions*, (1986) ed. M. Derrick (World Scientific, Singapore, 1987) p.365.
- [7] J. D. Bjorken, *Int. J. Mod. Phys.* **A7** (1992) 4189; *Phys. Rev.* **D47** (1993) 101; preprint SLAC-PUB-5823 (1992).
- [8] H. Murayama, I. Watanabe, and K. Hagiwara, KEK Report 91-11 (1992).
- [9] K. Hagiwara and D. Zeppenfeld, *Nucl. Phys.* **B274**, 1 (1986); *ibid.* **B313**, 560 (1989).
- [10] D. A. Dicus and R. Vega, *Phys. Rev. Lett.* **57**, 1110 (1986); *Phys. Rev.* **D37**, 2427 (1988); J. F. Gunion, J. Kalinowski, and A. Tofighi-Niaki, *Phys. Rev. Lett.* **57**, 2351 (1986); U. Baur and E. W. N. Glover, *Phys. Lett.* **B252**, 683 (1990).
- [11] S. S. D. Willenbrock and G. Valencia, *Phys. Lett.* **B247**, 341 (1990).
- [12] G. Peter Lepage, *J. Comput. Phys.* **27**, 192 (1978).
- [13] A. D. Martin, W. J. Stirling, and R. G. Roberts, *Phys. Lett.* **B306**, 145 (1993), erratum *ibid.***B309**, 492 (1993).

- [14] K. Hagiwara, S. Komamiya, and D. Zeppenfeld, *Z. Physik* **C29** 115 (1985); U. Baur, J. Vermaseren, and D. Zeppenfeld, *Nucl. Phys.* **B375**, 3 (1992).
- [15] V. Barger and R. J. N. Phillips, *Phys. Rev. Lett.* **55**, 2752 (1985); H. Baer, V. Barger, H. Goldberg, and R. J. N. Phillips, *Phys. Rev.* **D37**, 3152 (1988).
- [16] T. Han, G. Valencia, and S. S. D. Willenbrock, *Phys. Rev. Lett.* **69**, 3274 (1992).
- [17] Y. L. Dokshitzer, V. A. Khoze, and T. Sjöstrand, *Phys. Lett.* **B274** (1992) 116.
- [18] R. S. Fletcher and T. Stelzer, Univ. of Wisconsin preprint MAD/PH/763 (1993).
- [19] E. Gotsman, E. M. Levin, and U. Maor, *Phys. Lett.* **B309** (1993) 199.
- [20] H. Chehime and D. Zeppenfeld, *Phys. Rev.* **D47** (1993) 3898.
- [21] A. Duff, PhD thesis, Univ. of Wisconsin, Madison (1993).
- [22] D. Dicus, J. F. Gunion, and R. Vega, *Phys. Lett.* **B258**, 475 (1991); D. Dicus, J. F. Gunion, L. H. Orr, and R. Vega, *Nucl. Phys.* **B377**, 31 (1991).

TABLES

TABLE I. Values (in GeV) of the p_{tsa} parameter of Eq. (5) which are needed to match the cross sections at $\mathcal{O}(\alpha_s)$ with the lowest order results for the “ s -channel resonance” process. Values are given for two Higgs boson masses and different transverse momentum requirements for “visible” jets in pp collisions at $\sqrt{s} = 40$ TeV.

	1 jet inclusive		2 jet inclusive	
	$m_H = 500$ GeV	$m_H = 800$ GeV	$m_H = 500$ GeV	$m_H = 800$ GeV
$p_{Tj} > 20$ GeV	5.8	5.7	6.7	6.5
$p_{Tj} > 40$ GeV	6.1	5.9	7.9	7.6
$p_{Tj} > 60$ GeV	6.4	6.3	8.9	8.9

TABLE II. Cross sections (in fb) and central-jet-veto efficiencies ε for pp collisions at $\sqrt{s} = 40$ TeV. Only leptonic decays of both W 's ($W^\pm \rightarrow e^\pm \nu, \mu^\pm \nu$) are considered and the lepton and tagging jet cuts of Eqs. (12)–(14) are imposed, leaving $B \cdot \sigma(m_H = 800 \text{ GeV}) = 8.2(7.6)$ fb and $B \cdot \sigma(m_H = 100 \text{ GeV}) = 1.9(1.5)$ fb before central-jet-vetoing for the $\mathcal{O}(\alpha_s)$ (lowest order) calculation. A veto is imposed on central jets of $|\eta_j| < 3$ and transverse momenta $p_{Tj} > p_T^{\text{veto}}$ as given in the table. The signal is defined as the difference of the $m_H = 800 \text{ GeV}$ and $m_H = 100 \text{ GeV}$ cross sections.

a) 2 parton calculation				
	$B \cdot \sigma(m_H = 800 \text{ GeV})$	$B \cdot \sigma(m_H = 100 \text{ GeV})$	$B \cdot \sigma_{\text{signal}}$	ε
$p_T^{\text{veto}} = 20 \text{ GeV}$	4.4	0.5	3.8	0.62
30 GeV	4.5	0.5	4.0	0.65
40 GeV	4.7	0.6	4.1	0.67
60 GeV	5.1	0.6	4.5	0.73
b) 3 parton calculation				
	$B \cdot \sigma(m_H = 800 \text{ GeV})$	$B \cdot \sigma(m_H = 100 \text{ GeV})$	$B \cdot \sigma_{\text{signal}}$	ε
$p_T^{\text{veto}} = 20 \text{ GeV}$	3.4	0.2	3.1	0.50
30 GeV	3.6	0.2	3.4	0.54
40 GeV	3.8	0.2	3.6	0.57
60 GeV	4.3	0.3	3.9	0.62

FIGURES

FIG. 1. Representative Feynman graphs contributing to the electroweak process $pp \rightarrow W^+W^-jjjX$.

FIG. 2. Gap width distribution, $d\sigma/dy_{gap}$, in the electroweak process $pp \rightarrow W^+W^-jj(j)X$ at $\sqrt{s} = 40$ TeV. Results are shown for the full $\mathcal{O}(\alpha_s\alpha_{QED}^4)$ calculation and Higgs boson masses of $m_H = 800$ GeV (solid line) and $m_H = 100$ GeV (dashed line). The cuts of Eqs. (6)–(8) are imposed, including lepton acceptance cuts of $p_{T\ell} > 100$ GeV, $|\eta_\ell| < 2$. The cross section is normalized to include all W decay modes, however.

FIG. 3. Distribution in $\Delta\eta_{sj}$, the minimum pseudorapidity separation of the third (typically soft) parton from the two jets defining the boundary of the gap region. Negative values of $\Delta\eta_{sj}$ correspond to the emission of a soft parton ($p_T < 40$ GeV) into the gap region. Curves are shown for the same parameters as in Fig. 2.

FIG. 4. Normalized gap width distribution, $d\sigma/dz$ (see Eq. (11)), for $W^+W^-jj(j)X$ events in pp collisions at $\sqrt{s} = 40$ TeV. $z = 0$ corresponds to the center of the gap and $z = \pm 1$ mark the gap edges. As in Fig. 2 the cross sections are normalized to include all W decay modes. Results are shown for $m_H = 800$ GeV (solid line) and $m_H = 100$ GeV (dashed line) and the cuts of Eqs. (6)–(8) are imposed.

FIG. 5. Pseudorapidity distribution of the tagging jet candidate (the most energetic jet of $p_{Tj} > 40$ GeV) in $pp \rightarrow W^+W^-j(jj)X$ events at $\sqrt{s} = 40$ TeV. Curves are shown for 1-jet inclusive events at $\mathcal{O}(\alpha_s)$ and Higgs boson masses of $m_H = 800$ GeV (solid line) and $m_H = 100$ GeV (dashed line). The acceptance cuts of Eq. (12) and Eq. (13) are imposed and the curves are normalized as in Fig. 2.

FIG. 6. Transverse momentum distribution of the tagging jet candidate in $pp \rightarrow W^+W^-j(jj)X$ events at $\sqrt{s} = 40$ TeV. Acceptance cuts and normalization of the curves are as in Fig. 5.

FIG. 7. Pseudorapidity distribution of the veto-jet candidate in $pp \rightarrow W^+W^-j(jj)X$ events at $\sqrt{s} = 40$ TeV. Curves are shown for 1-jet inclusive events at $\mathcal{O}(\alpha_s)$ and Higgs boson masses of $m_H = 800$ GeV (solid line) and $m_H = 100$ GeV (dashed line). In addition to the acceptance cuts as imposed in Figs. 5 and 6 the presence of a tagging jet of $p_{Tj} > 40$ GeV, $E_j > 1$ TeV is required in the pseudorapidity range $3 < |\eta_{j,\text{tag}}| < 5$. The curves are normalized as in Fig. 2.

FIG. 8. Feynman diagrams corresponding to amplitudes \mathcal{M}_1 through \mathcal{M}_3 . \mathcal{M}_3 is obtained from \mathcal{M}_2 by interchanging the W^+ and W^- lines in graph b). The crosses mark the four locations where the external gluon must be attached, leading to a total of eight permutations for graph b).

FIG. 9. Feynman diagrams corresponding to amplitudes \mathcal{M}_4 through \mathcal{M}_7 . The circles represent the four-boson-vertices as well as s -, t - and/or u -channel electroweak boson exchange which, in HELAS, are combined into a single subroutine.

FIG. 10. Feynman diagrams corresponding to amplitudes \mathcal{M}_8 through \mathcal{M}_{35} . The permutations involve the different attachments of the final state W 's to the lower quark line, the interchange of final state W^+ and W^- , the interchange of upper and lower quark line, and the different attachments of the gluon.

FIG. 11. Feynman diagrams corresponding to amplitudes \mathcal{M}_{36} through \mathcal{M}_{55} . In determining the number of permutations, γ and Z exchange are not counted separately.

FIG.

12.

Feynman diagrams corresponding to amplitudes \mathcal{M}_{56} through \mathcal{M}_{67} .

This figure "fig1-1.png" is available in "png" format from:

<http://arxiv.org/ps/hep-ph/9312357v1>

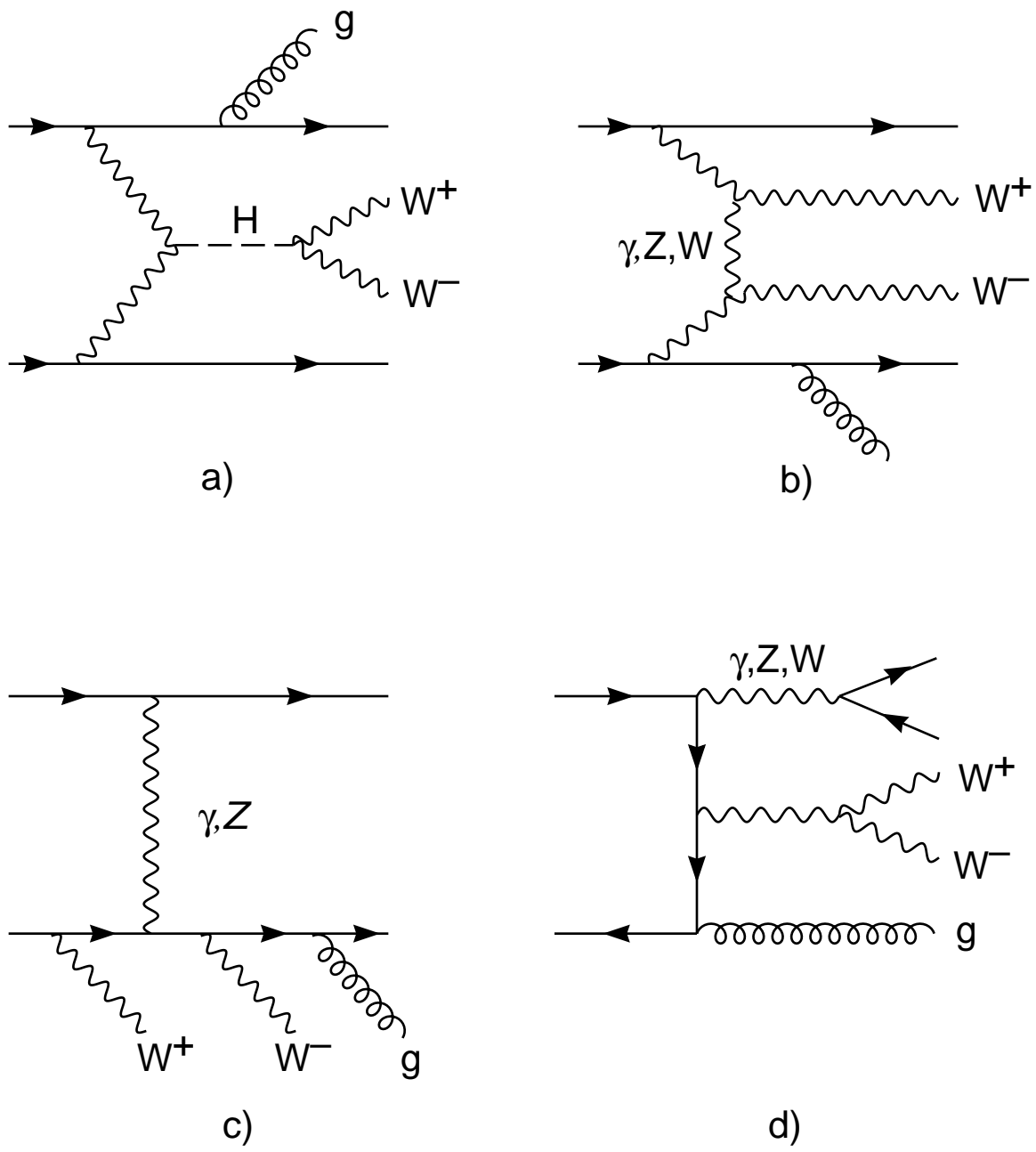


Fig. 1

This figure "fig2-1.png" is available in "png" format from:

<http://arxiv.org/ps/hep-ph/9312357v1>

This figure "fig3-1.png" is available in "png" format from:

<http://arxiv.org/ps/hep-ph/9312357v1>

This figure "fig1-2.png" is available in "png" format from:

<http://arxiv.org/ps/hep-ph/9312357v1>

This figure "fig2-2.png" is available in "png" format from:

<http://arxiv.org/ps/hep-ph/9312357v1>

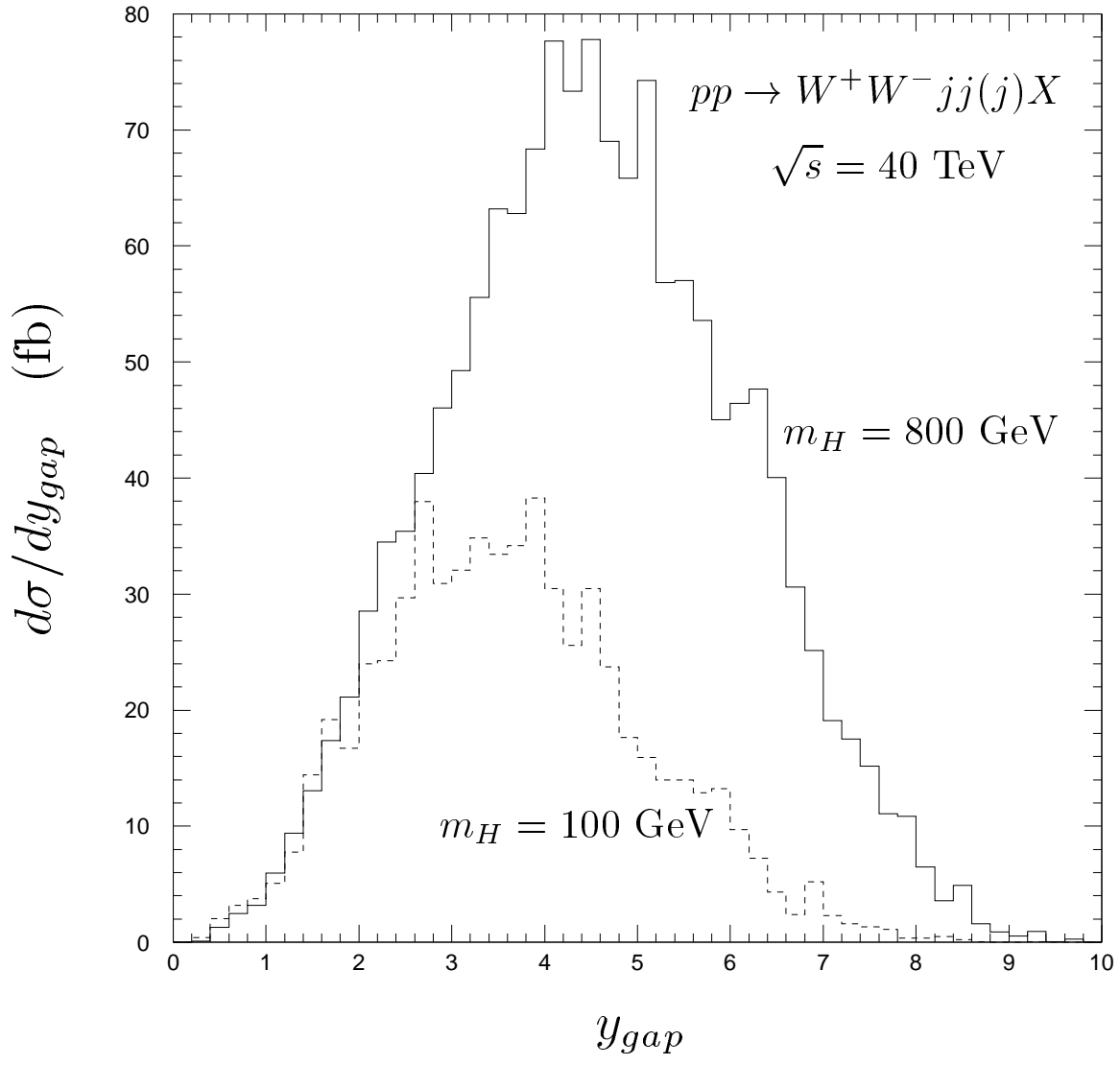


Fig. 2

This figure "fig3-2.png" is available in "png" format from:

<http://arxiv.org/ps/hep-ph/9312357v1>

This figure "fig1-3.png" is available in "png" format from:

<http://arxiv.org/ps/hep-ph/9312357v1>

This figure "fig2-3.png" is available in "png" format from:

<http://arxiv.org/ps/hep-ph/9312357v1>

This figure "fig3-3.png" is available in "png" format from:

<http://arxiv.org/ps/hep-ph/9312357v1>

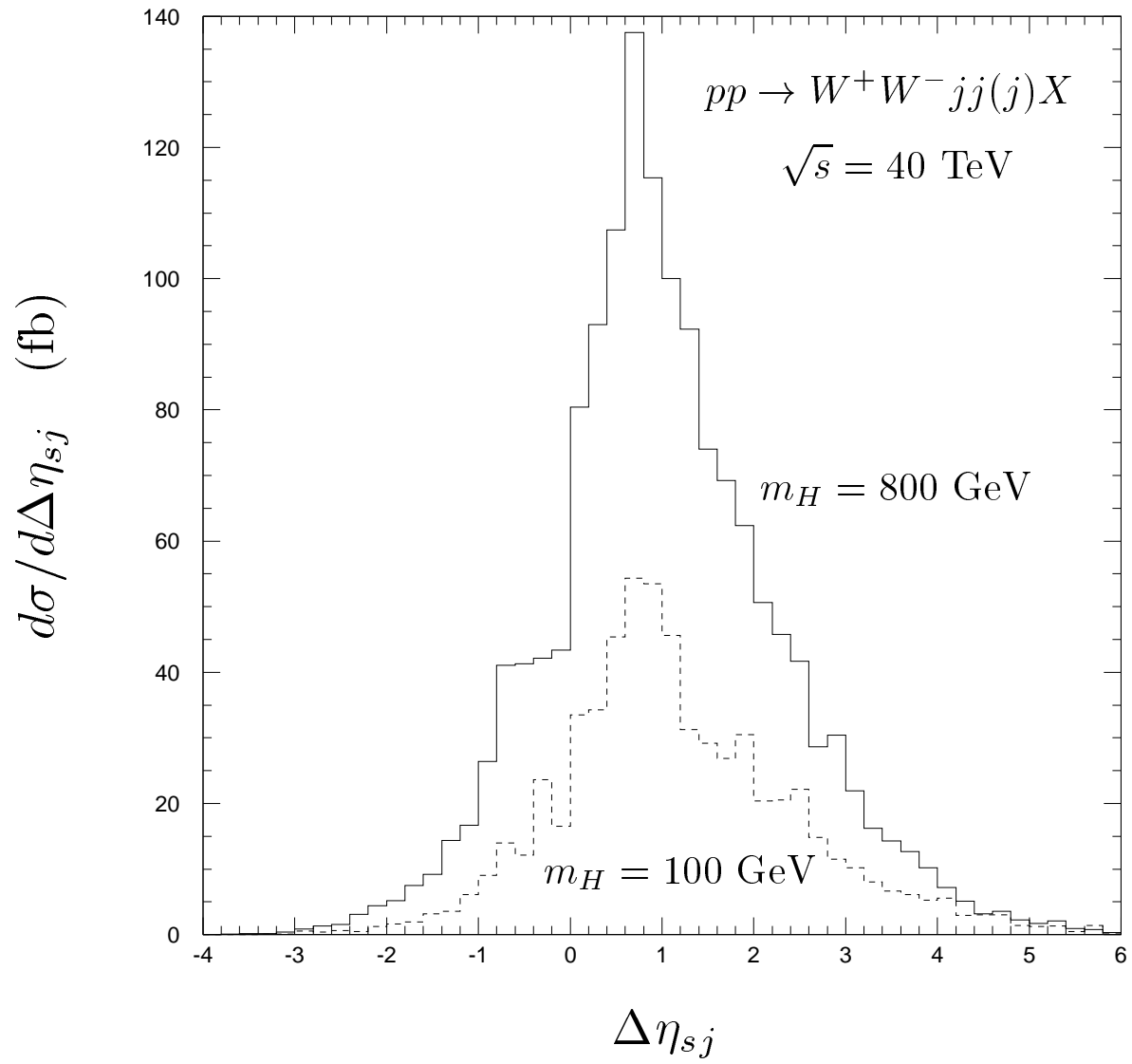


Fig. 3

This figure "fig1-4.png" is available in "png" format from:

<http://arxiv.org/ps/hep-ph/9312357v1>

This figure "fig2-4.png" is available in "png" format from:

<http://arxiv.org/ps/hep-ph/9312357v1>

This figure "fig3-4.png" is available in "png" format from:

<http://arxiv.org/ps/hep-ph/9312357v1>

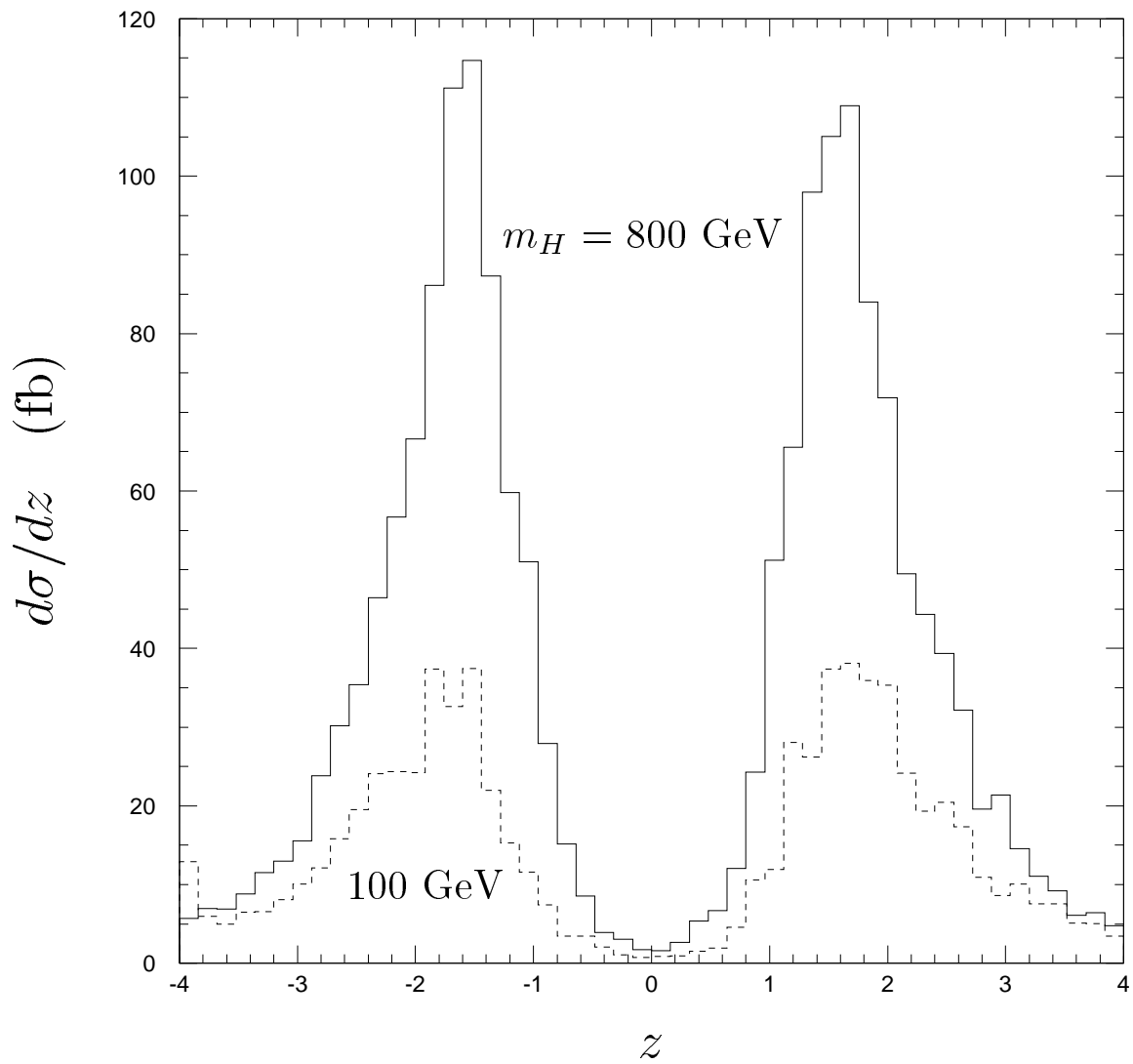


Fig. 4

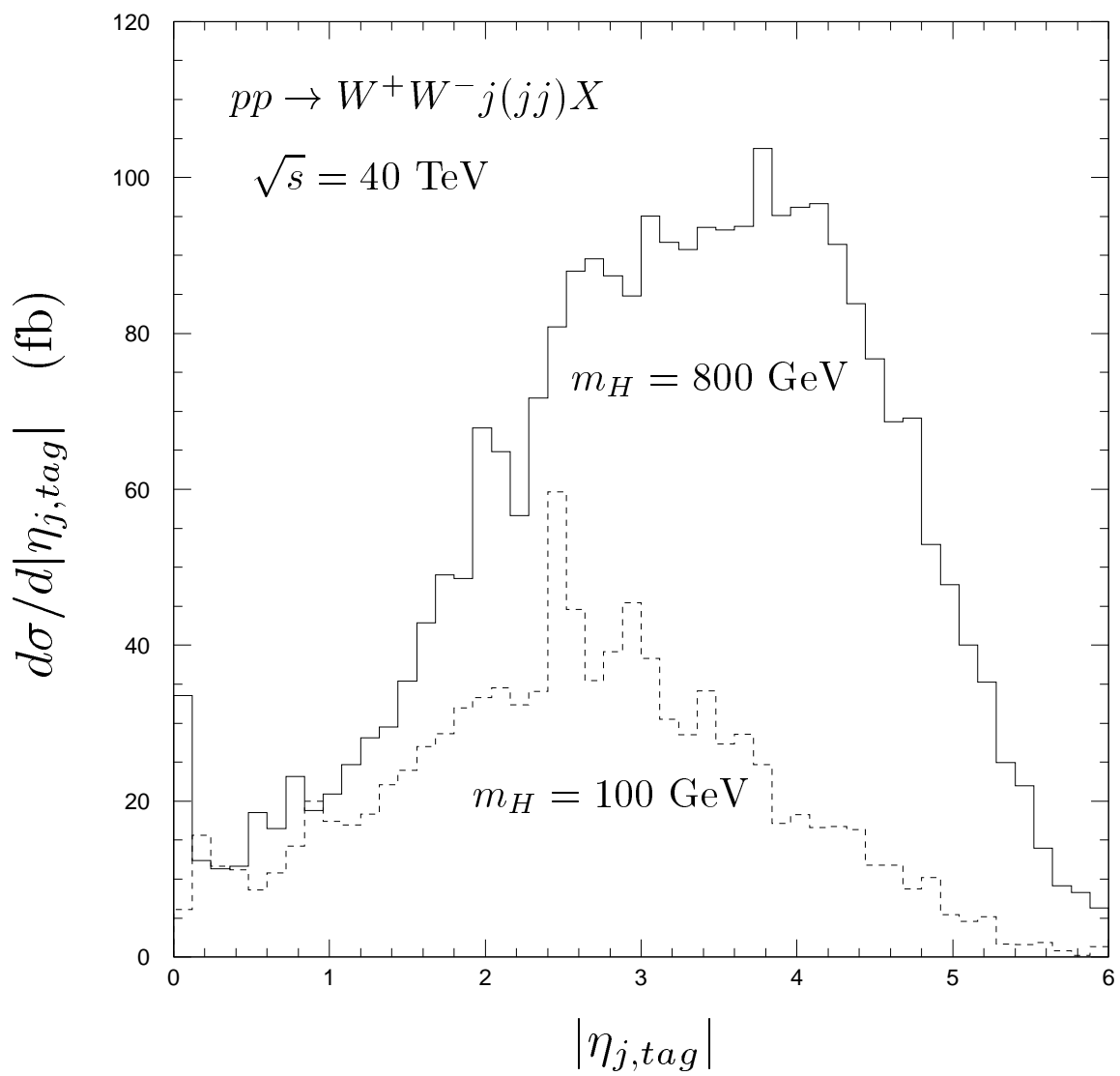


Fig. 5

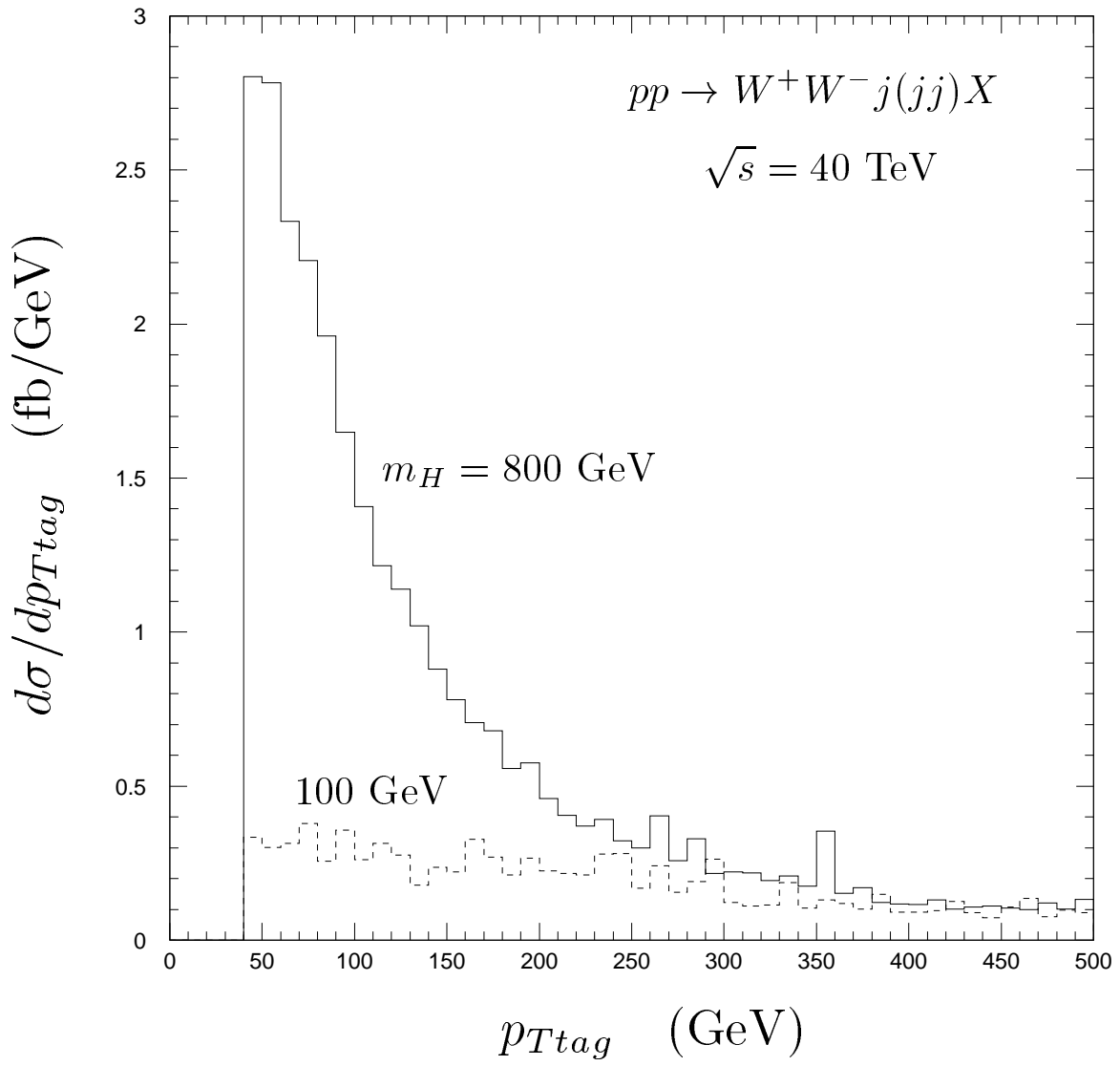


Fig. 6

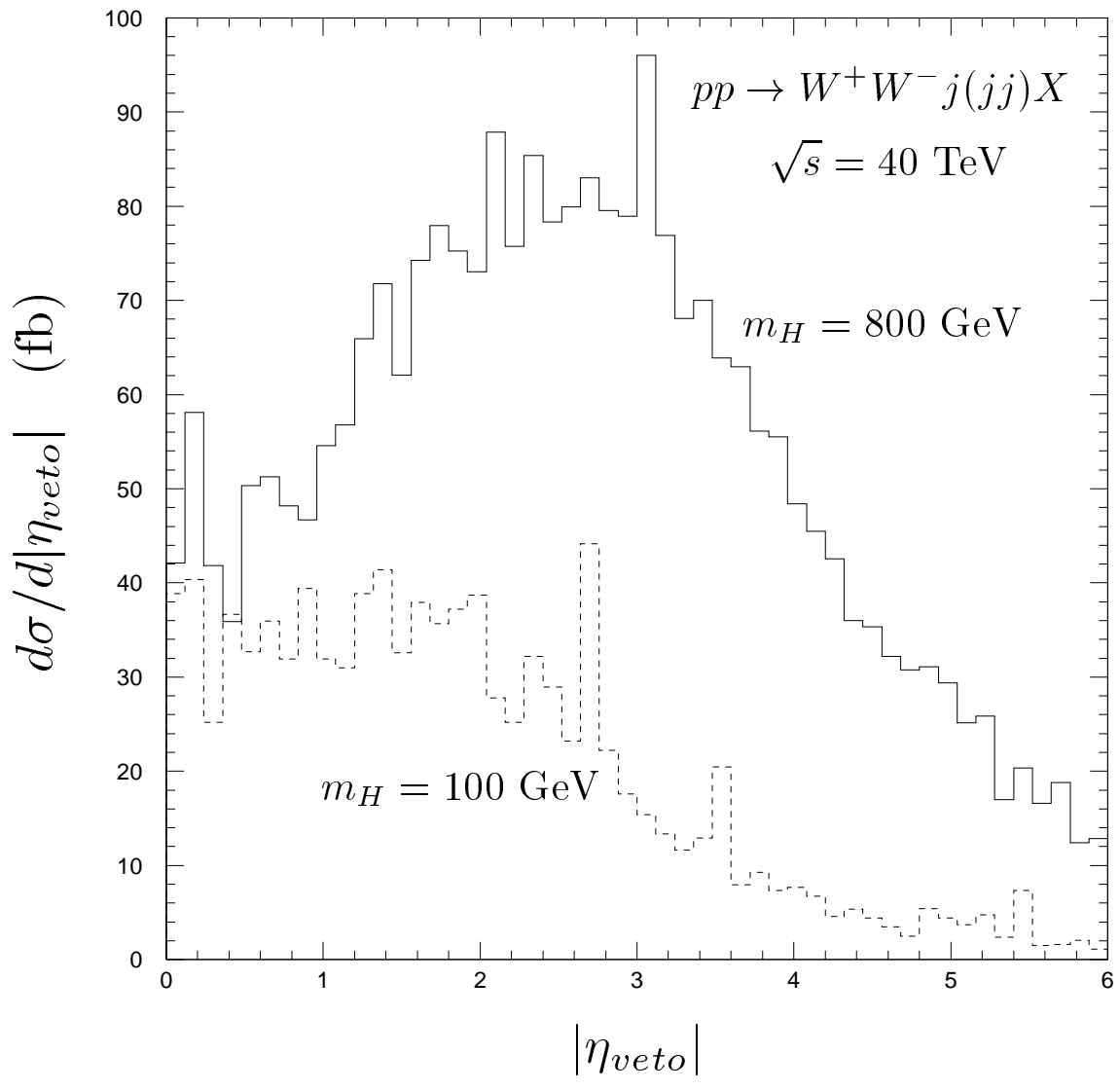


Fig. 7

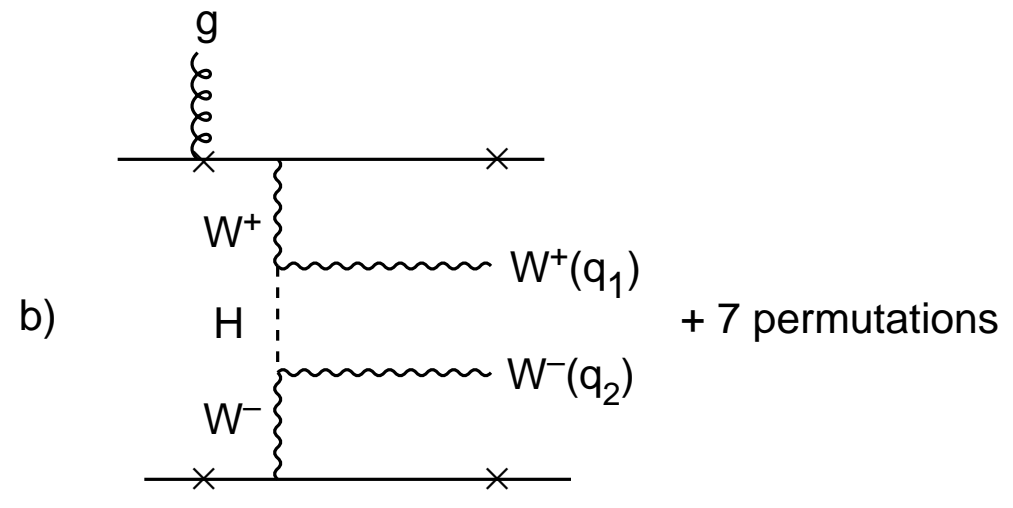
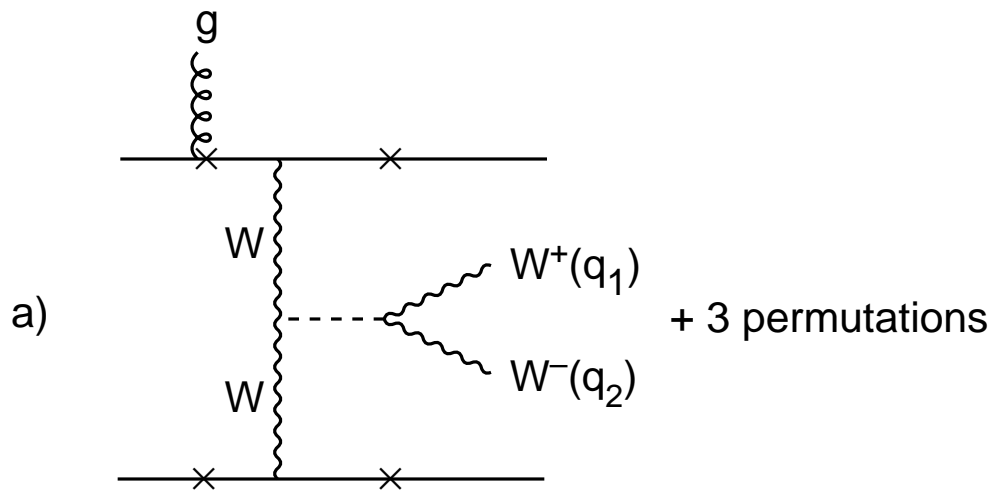


Fig. 8

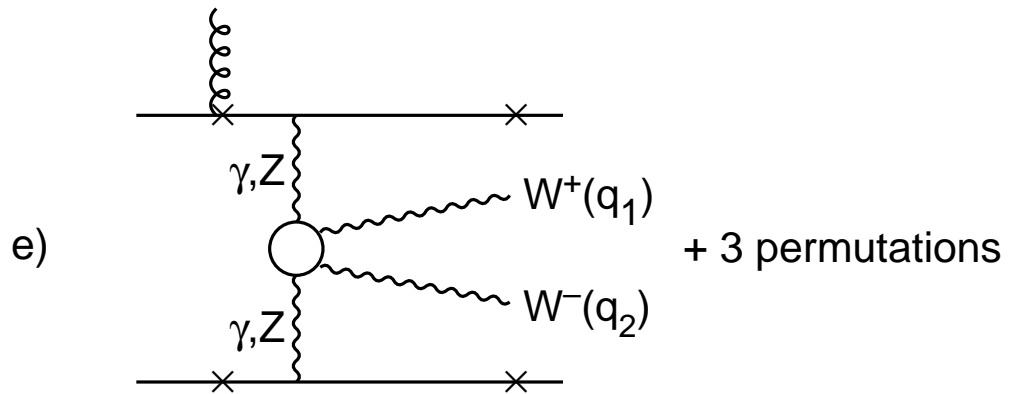
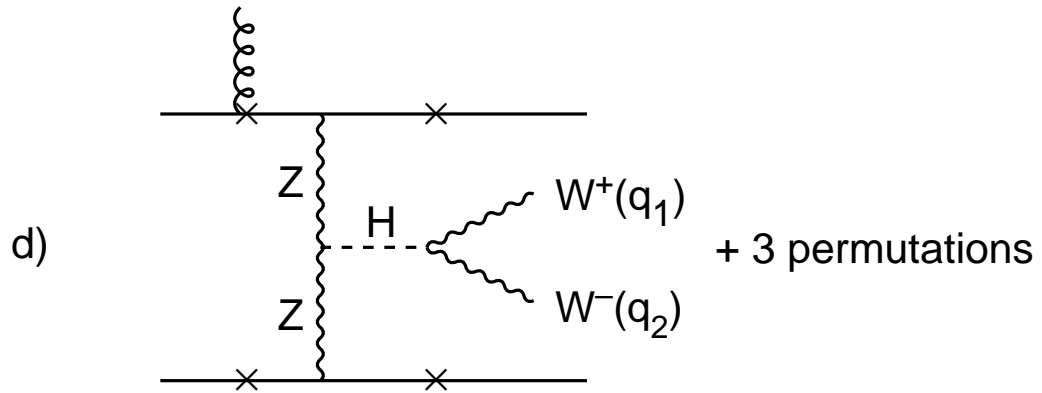
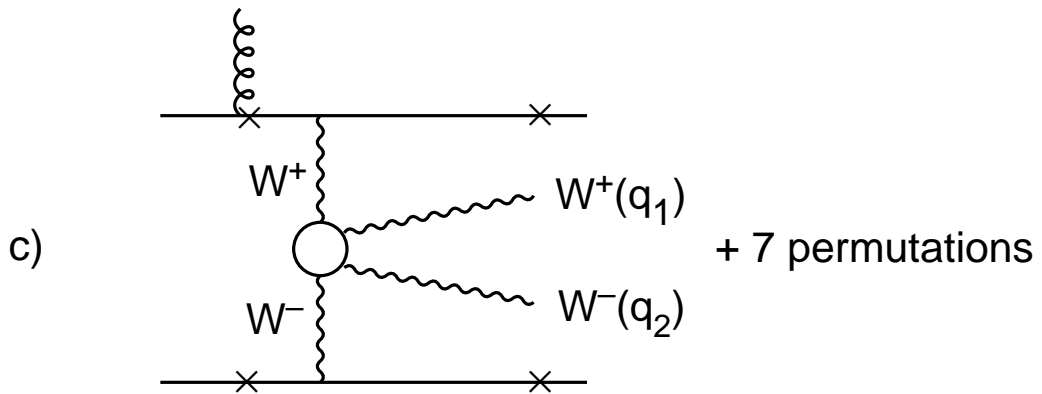


Fig. 9

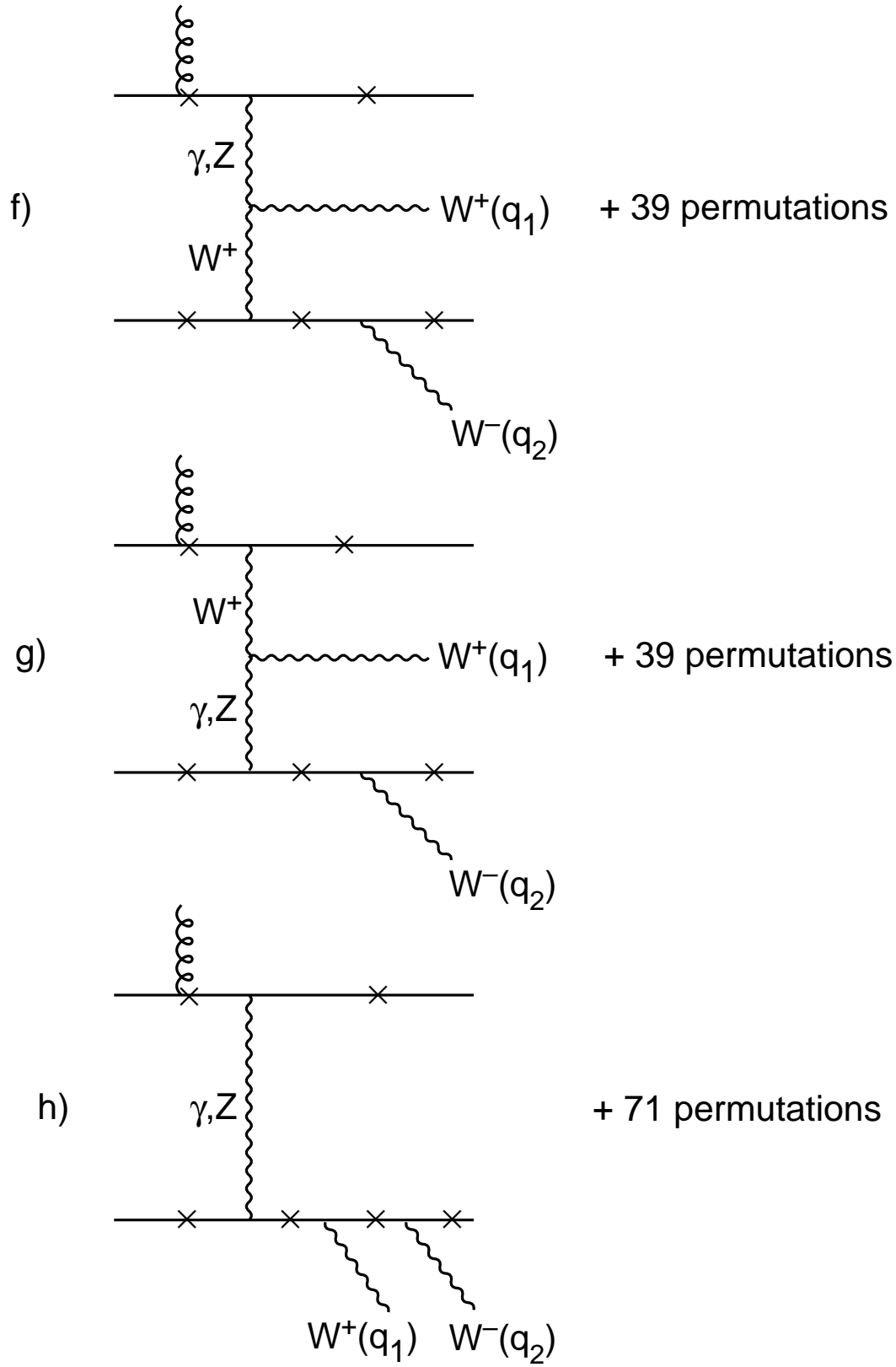


Fig. 10

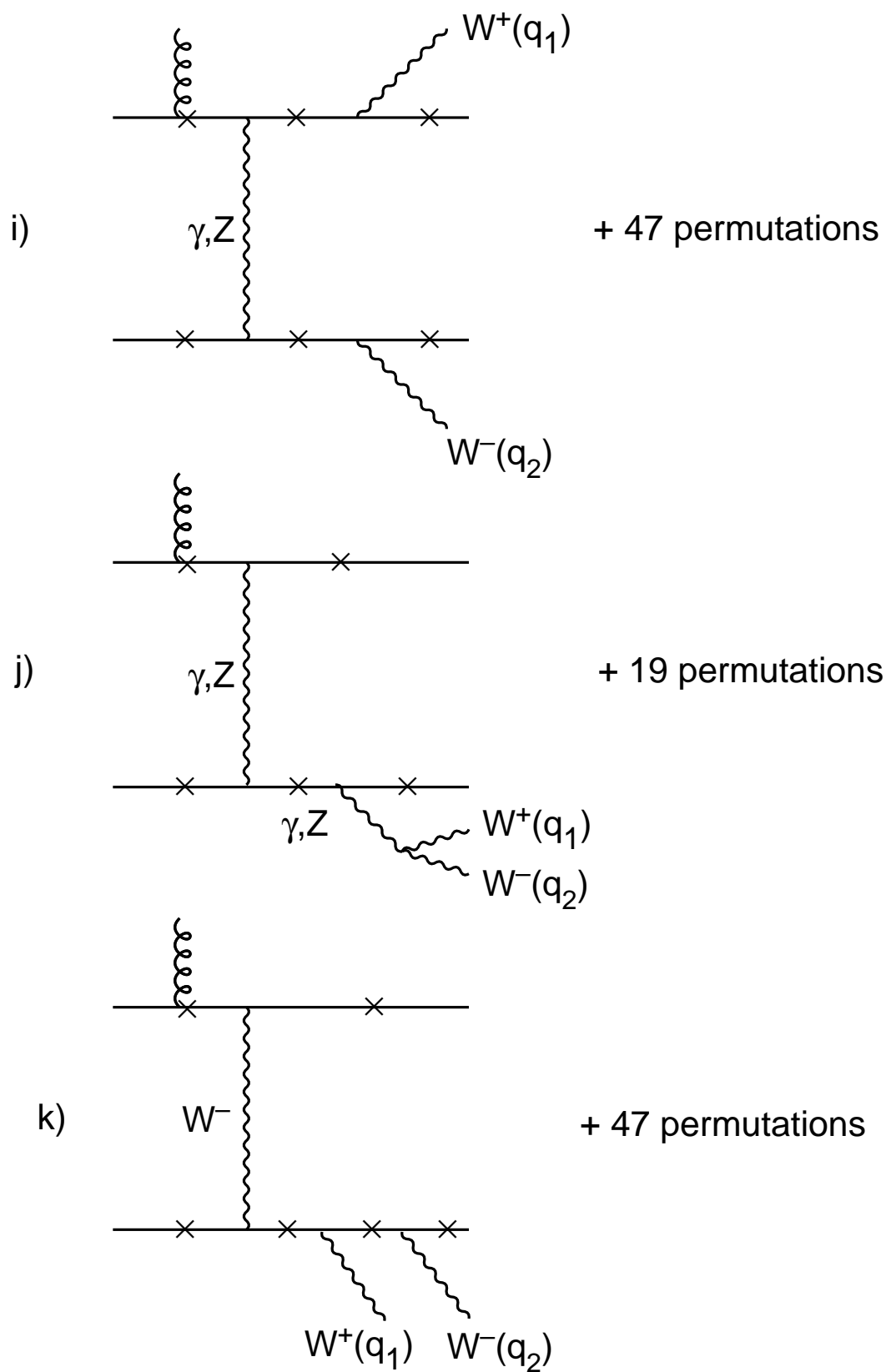


Fig. 11

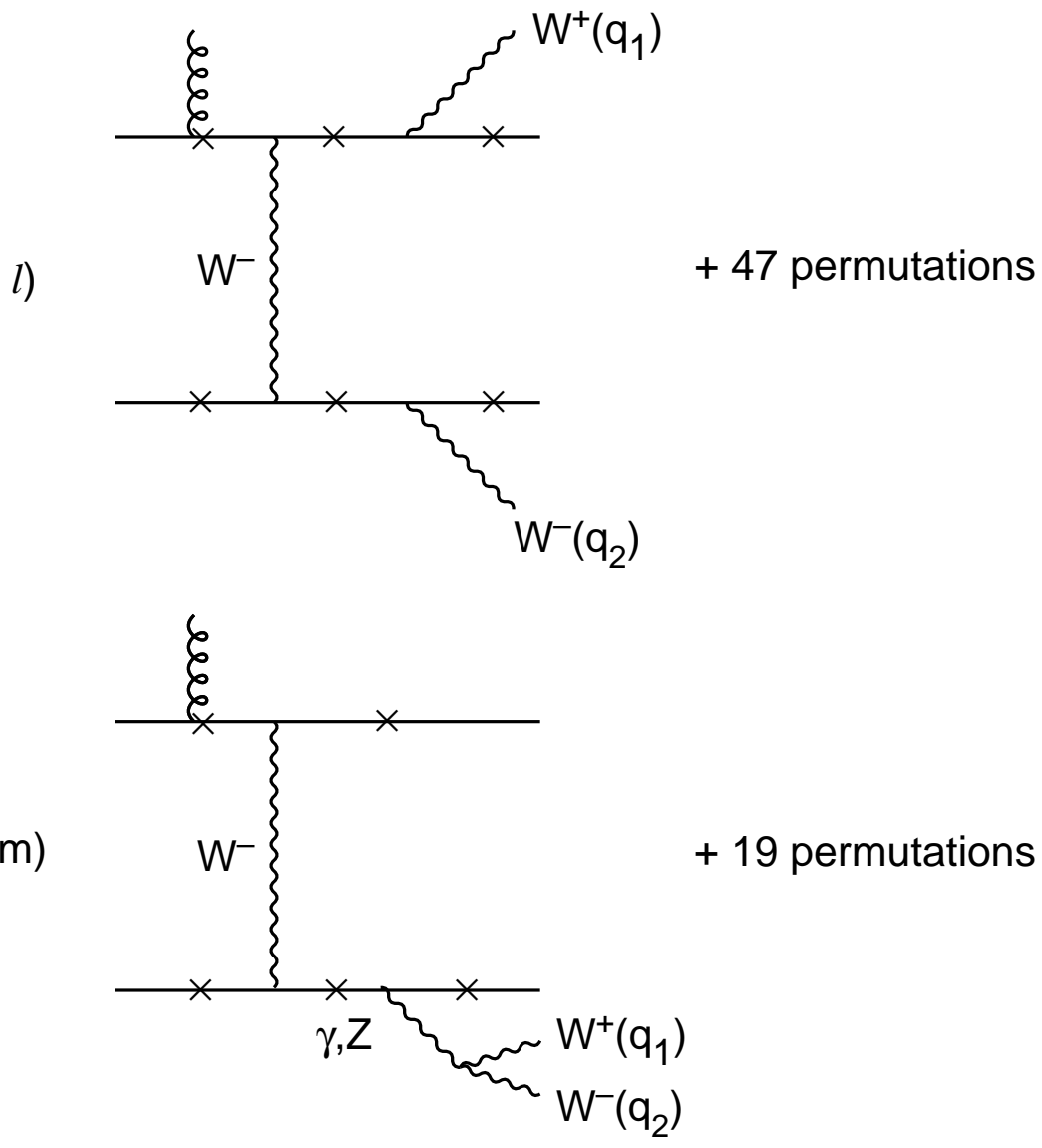


Fig. 12